



ISTITUTO NAZIONALE DI RICERCA METROLOGICA Repository Istituzionale

Hysteresis losses and specific absorption rate measurements in magnetic nanoparticles for hyperthermia applications

This is the author's submitted version of the contribution published as:

Original

Hysteresis losses and specific absorption rate measurements in magnetic nanoparticles for hyperthermia applications / Coisson, Marco; Barrera, Gabriele; Celegato, Federica; Martino, Luca; Kane, Shashank N.; Raghuvanshi, Saroj; Vinai, Franco; Tiberto, Paola. - In: BIOCHIMICA ET BIOPHYSICA ACTA-GENERAL SUBJECTS. - ISSN 0304-4165. - 1861:6(2017), pp. 1545-1558. [10.1016/j.bbagen.2016.12.006]

Availability:

This version is available at: 11696/57470 since: 2018-02-27T13:25:51Z

Publisher:

Elsevier

Published

DOI:10.1016/j.bbagen.2016.12.006

Terms of use:

This article is made available under terms and conditions as specified in the corresponding bibliographic description in the repository

Publisher copyright

(Article begins on next page)

Hysteresis losses and specific absorption rate measurements in magnetic nanoparticles for hyperthermia applications

Marco Coïsson^{1,*}, Gabriele Barrera¹, Federica Celegato¹, Luca Martino¹,
Shashank N. Kane², S. Raghuvanshi², Franco Vinai¹, and Paola Tiberto¹

¹*INRIM, strada delle Cacce 91, 10135 Torino (TO), Italy and*

²*School of Physics, Devi Ahilya University, Indore, India*

* Corresponding author: m.coisson@inrim.it

ABSTRACT

Background. Magnetic hysteresis loops areas and hyperthermia on magnetic nanoparticles have been studied with the aim of providing reliable and reproducible methods of measuring the specific absorption rate (SAR).

Methods. The SAR of Fe_3O_4 nanoparticles with two different mean sizes, and $\text{Ni}_{1-x}\text{Zn}_x\text{Fe}_2\text{O}_4$ ferrites with $0 \leq x \leq 0.8$ has been measured with three approaches: static hysteresis loops areas, dynamic hysteresis loops areas and hyperthermia of a water solution. For dynamic loops and thermometric measurements, specific experimental setups have been developed, that operate at comparable frequencies (≈ 69 kHz and ≈ 100 kHz respectively) and rf magnetic field peak values (up to 100 mT). The hyperthermia setup has been fully modelled to provide a direct measurement of the SAR of the magnetic nanoparticles by taking into account the heat exchange with the surrounding environment in non-adiabatic conditions and the parasitic heating of the water due to ionic currents.

Results. Dynamic hysteresis loops are shown to provide an accurate determination of the SAR except for superparamagnetic samples, where the boundary with a blocked regime could be crossed in dynamic conditions. Static hysteresis loops consistently underestimate the specific absorption rate but can be used to select the most promising samples.

Conclusions. A means of reliably measure SAR of magnetic nanoparticles by different approaches for hyperthermia applications is presented and its validity discussed by comparing different methods.

General Significance. This work fits within the general subject of metrological traceability in medicine with a specific focus on magnetic hyperthermia.

I. INTRODUCTION

Magnetic particles hyperthermia is a branch of hyperthermia [1–4] where magnetic nanoparticles are employed thanks to their ability to exploit not only the electric, but also the magnetic component of the electromagnetic field used to excite them. In spite of the significant advantages that magnetic hyperthermia could bring [5–7], which include being non invasive and enhancing the effects of chemotherapy and radiotherapy [8], it has not yet reached clinical applications, as many open questions still need to be addressed. These include the ability to properly characterize the physical properties of the employed magnetic nanoparticles in conditions comparable to those of hyperthermia treatments, where specific power losses may be significantly different than those obtained in typical laboratory conditions [9, 10], and measuring reliable specific absorption rate values [11]. Therefore, many researchers have concentrated on this subject in last years [12, 13]. These have addressed the open issues from the point of view of the magnetic material optimization in terms of particles microstructure [14–16], of new particles types [17–21], of combined physical properties that enhance the heating power or versatility of the nanoparticles [22, 23], or of improved setups for hyperthermia characterizations and specific absorption rate measurements [11, 24–26].

However, the subject is far from having been comprehensively investigated, as several open issues still require significant efforts from the scientific community. In particular, we would like to focus the attention to the necessity of reliably measuring specific absorption rate (SAR) values, with a rigorous determination of the uncertainty and traceability to national standards, in laboratory conditions, as the current broad range of custom hyperthermia setups and the lack of validated protocols and calibrants makes SAR measurements difficult, if not impossible, to compare [27]. This issue falls into the more general category of the traceability assessment in medicine [28–30], a subject that has been under debate in the last two decades. To this regard, a metrological framework for the measurement of SAR will have to address at least three problems: (i) the development of hyperthermia setups that allow traceable and correctly defined measurements of the specific absorption rate of magnetic nanoparticles in non adiabatic conditions; (ii) the development of measurement setups that allow the measurement of the particles dynamic magnetic properties upon which the heating effect in hyperthermia treatments depends; (iii) the realization of reference colloidal suspensions of nanoparticles that can be used to test or, possibly, calibrate hyperthermia

experiments. The achievement of all these medium-to-long term goals is necessary as hyperthermia treatments will eventually be applied to human patients, therefore requiring an extremely careful choice of the magnetic materials to be exploited, and a well calibrated dose of electromagnetic radiation to which the human body is exposed.

In this context, in this paper we approach the problem of the measurement of the specific absorption rate and of the dynamic magnetic properties of magnetic nanoparticles by comparing three different experimental methods: measurement of the static hysteresis loops areas, measurement of dynamic hysteresis loops areas at frequency and magnetic field peak values comparable to those exploited in hyperthermia treatments, and direct measurement of SAR in a hyperthermia setup. Whereas the last method is meant to establish a protocol for the accurate characterization and modelling of an hyperthermia system and to a proper definition of its measurand in non adiabatic conditions, the measurement of the magnetic properties of the nanoparticles in dynamic conditions (in field and frequency ranges comparable to hyperthermia experiments) is a required step for the understanding of the physical mechanisms of magnetic losses in magnetic nanoparticles, that have been shown to depend on the material [31, 32], particles size [32–34] and aggregation state [34]. To this purpose, a B-H loop tracer operating at ≈ 69 kHz at applied fields up to 60 mT has been developed and calibrated, and will be described. Then, a hyperthermia setup operating in non-adiabatic conditions has been developed, characterized experimentally and modelled thermodynamically. Magnetite and Ni-Zn ferrites nanoparticles will be investigated. The advantages and disadvantages of the three methods for SAR determination, and their sources of discrepancy, will be presented and discussed.

II. EXPERIMENTAL

II.1. Samples

Fe_3O_4 nanoparticles (sample P1) having a nominal diameter in the range 10 – 20 nm have been obtained by Politronica s.r.l., whereas a second batch of Fe_3O_4 nanoparticles (sample P2) with a nominal diameter in the range 20 – 30 nm has been obtained by Alfa Aesar. Sample P1 is superparamagnetic at room temperature, whereas sample P2 reports a coercive field of ≈ 100 Oe. Their static hysteresis loops measured by means of a vibrating

sample magnetometer (VSM) are shown in Fig. 1.

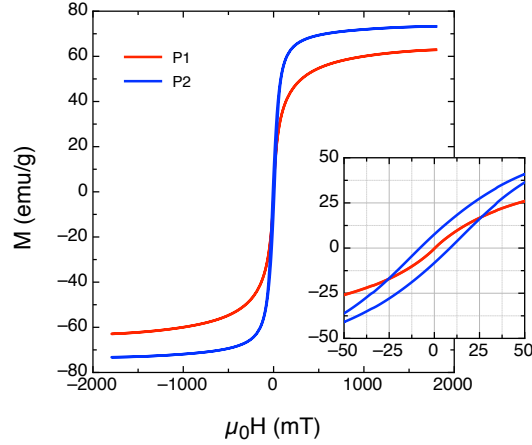


FIG. 1. Static hysteresis loops of samples P1 and P2. Inset: magnification at low fields to put in evidence the coercivity.

Polycrystalline spinel ferrites nanoparticles have been recently considered for hyperthermia applications [35, 36] because of their versatility; among these, Ni-Zn ferrites have attracted significant interest because of their easily tunable magnetic properties and sufficient biocompatibility [37, 38]. In this work Ni-Zn ferrites having composition $\text{Ni}_{1-x}\text{Zn}_x\text{Fe}_2\text{O}_4$ ($0 \leq x \leq 0.8$) have been synthesized by a sol-gel autocombustion technique [39]. As the as-burnt particles already display reasonably good magnetic properties, no calcination at high temperature is required to transform the dried gel into the final powder with the expected crystal structure. Therefore, a significant energy saving can be obtained with this synthesis technique. XRD patterns on the Ni-Zn ferrites samples confirm the formation of a single phase nano-crystalline cubic spinel structure, independent on the composition, with small amounts of residual Fe_2O_3 . XRD spectra for the studied Ni-Zn ferrites samples are reported in Fig. 2, from which average crystallite size is calculated. A summary of the nomenclature of all the studied samples is reported in Table I, together with the particles / crystallites sizes and cation information (for Ni-Zn ferrites).

Following the procedure described in [40], from XRD data the cation distribution in the A- and B- sites has been derived for the Ni-Zn ferrites, as a function of the Zn content. The results are summarized in Table I. As it turns out, Ni strongly prefers the B-site, whereas Zn should strongly prefer the A-site [41, 42]. In our case, the absence of high-temperature post-annealing induces a non-equilibrium cation distribution for Zn occupying both A- and

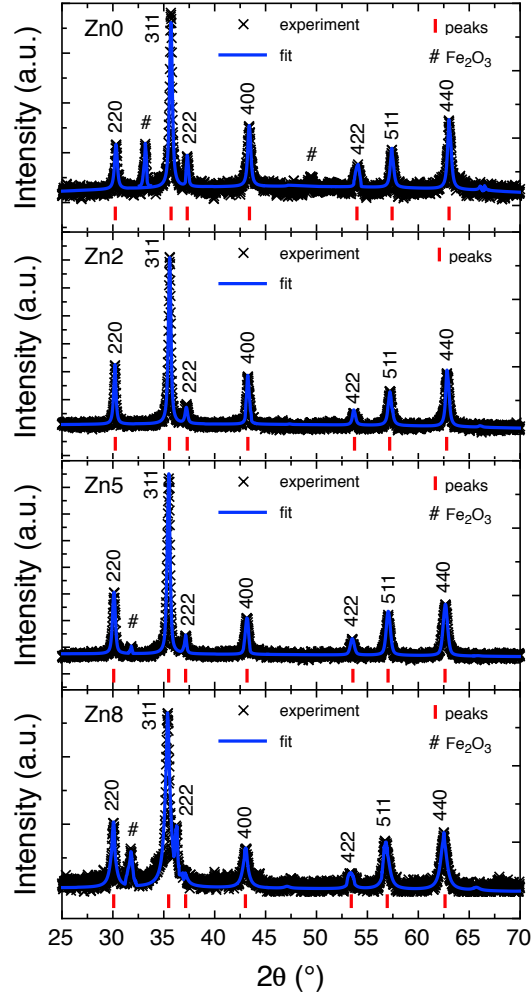


FIG. 2. XRD patterns of Ni-Zn ferrites powder samples.

B- sites with a preference for the latter when the content of Zn is large. When both Ni and Zn are present, Ni forces Zn to the A-site for low values of concentration, and only when Ni begins to be replaced by Zn its occupancy of the B-site becomes significant. This non monotonous evolution of the cationic distribution with composition significantly affects their static hysteresis loops, measured with a VSM, that are shown in Fig. 3. Indeed, the saturation magnetization has a maximum for the Zn2 sample, whereas the coercive field has an apparently decreasing trend with Zn content, although not well defined, the sample Zn0 displaying the highest coercive field anyway. A detailed correlation of the microstructure of these Ni-Zn ferrites with their magnetic properties is out of the scope of this work.

Sample name	Composition	Size	Cation distribution
P1	Fe_3O_4	10 – 20 nm	
P2	Fe_3O_4	50 – 100 nm	
Zn0	NiFe_2O_4	33.6 nm	A-site: $\text{Fe}_{1.0}^{3+}$ B-site: $\text{Ni}_{1.0}^{2+}\text{Fe}_{1.0}^{3+}$
Zn2	$\text{Ni}_{0.8}\text{Zn}_{0.2}\text{Fe}_2\text{O}_4$	32.7 nm	A-site: $\text{Ni}_{0.30}^{2+}\text{Zn}_{0.18}^{2+}\text{Fe}_{0.52}^{3+}$ B-site: $\text{Ni}_{0.50}^{2+}\text{Zn}_{0.02}^{2+}\text{Fe}_{0.48}^{3+}$
Zn5	$\text{Ni}_{0.5}\text{Zn}_{0.5}\text{Fe}_2\text{O}_4$	27.6 nm	A-site: $\text{Ni}_{0.1}^{2+}\text{Zn}_{0.35}^{2+}\text{Fe}_{0.55}^{3+}$ B-site: $\text{Ni}_{0.4}^{2+}\text{Zn}_{0.15}^{2+}\text{Fe}_{0.45}^{3+}$
Zn8	$\text{Ni}_{0.2}\text{Zn}_{0.8}\text{Fe}_2\text{O}_4$	22.9 nm	A-site: $\text{Zn}_{0.15}^{2+}\text{Fe}_{0.85}^{3+}$ B-site: $\text{Ni}_{0.2}^{2+}\text{Zn}_{0.65}^{2+}\text{Fe}_{0.15}^{3+}$

TABLE I. List of measured samples, indicating their conventional name and composition, particles size and cation distribution (for Ni-Zn).

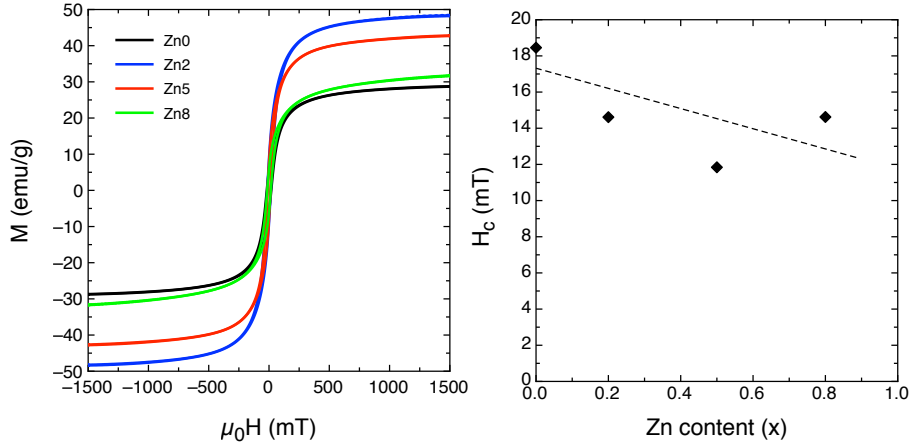


FIG. 3. Left: static hysteresis loops of samples samples Zn0 through Zn8. Right: dependence of coercive field with Zn content; the dashed line is a guide to the eye.

II.2. Hyperthermia setup

A hyperthermia setup consists of a rf coil generating an electromagnetic field in which a water solution of the studied magnetic particles is immersed. A thermometer measures the time-dependent temperature variation of the solution during the application of the electromagnetic field and after it has been switched off. A hyperthermia setup has been developed in our laboratory with the aim of performing hyperthermia measurements in non adiabatic conditions. In order to make measurements reliable, a thorough investigation of the setup

is required in order to develop an accurate thermodynamic model. A preliminary version has been described in [25]; with respect to that, the current setup has been significantly improved, and its model equations consequently updated. Therefore, its complete description, characterization and modelling will be given in the following.

A schematic representation of the hyperthermia setup is shown in Fig. 4. An eppendorf tube contains the water-dispersed magnetic nanoparticles, with the desired concentration. The volume of the solution is set to 1 mL. The eppendorf tube is held in place by a quartz sample holder that is also filled with water, whose role is to act as a thermostat against quick temperature variations in the surrounding environment. The quartz holder has a significantly large volume, approximately 70 mL, of which 12 mL surround the eppendorf tube in the region that is located inside the exciting rf coil. This consists of a copper pipe wound in 4 turns; inside the coil, a water flow keeps the temperature at 23 ± 1 °C. The rf coil is excited by a 10 kW resonant power supply coupled with a matching network, and generates an electromagnetic field with a frequency of ≈ 100 kHz and an amplitude of its magnetic component in the 0–100 mT range. According to [43], at an operating frequency of ≈ 100 kHz the magnetic field should not exceed ≈ 60 mT during hyperthermia treatments; in the following, this will be treated as the upper limit for hyperthermia measurements.

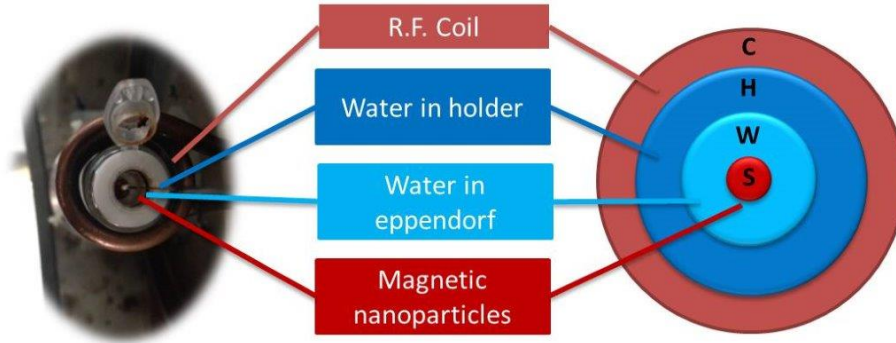


FIG. 4. Schematic representation of the hyperthermia setup, with its main components depicted in different colours and associated to the corresponding element in the photograph.

The temperature of the water solution containing the magnetic particles is measured by means of a fiber-optic fluorescence thermometer, that can be operated under the application of the rf field without electromagnetic interference and without contributing to the heating of the sample. Real-time acquisition of the temperature of the water solution in the eppendorf tube is therefore possible with the rf field switched both on and off.

The aim of an hyperthermia setup is to measure the specific absorption rate (SAR) of the magnetic nanoparticles dispersed in the water solution while they are exposed to the exciting rf electromagnetic field. As this is a measurement of power, a calorimetric measurement would be advisable [44]; however, this approach is usually quite complex. A simpler approach consists in assuming negligible heat exchange between the experimental setup and the surrounding environment (adiabatic approximation); this condition can be achieved mostly by reducing the measurement time to just a few seconds after the rf field has been switched on. The initial slope of the temperature vs. time curve is then used to estimate the SAR under the assumption of adiabatic conditions [45]. In our case [25], as with other experiments as well [11], the experimental setup is instead considered as non-adiabatic, but its heat exchange with the surrounding environment is thoroughly investigated and modelled. As a result, the SAR measurement will come from a complete description of the whole time evolution of the temperature of the water solution in the eppendorf tube, during the heating process when the rf field is on, and during the cooling process after it has been switched off. As we will see in the following, a thermodynamical model will be used to reproduce the temperature vs. time experimental curves; the model will contain only physical quantities that have been measured during the calibration and system's characterization phase, having as the only free parameter the power released by the hyperthermia source (i.e. the magnetic nanoparticles). This parameter will be adjusted to reproduce the experimental curve, and will therefore provide a direct measurement of the SAR of the particles.

The modelling of the experimental setup takes into account the heat exchanged between its various components and the surrounding environment. The magnetic nanoparticles excited by the rf electromagnetic field provide the source term of heat, whose time variation $\frac{\delta Q_s}{dt} = \frac{\delta Q_{s,out}}{dt}$ equals the amount of heat per unit time that is transferred to the water in the solution. As a consequence, the water contained in the eppendorf tube receives an amount of heat $Q_{w,in}$, and in turns exchanges heat $Q_{w,out}$ with the quartz holder filled with water. Similarly, the quartz holder receives heat ($Q_{h,in}$) from the eppendorf tube and releases energy ($Q_{h,out}$) to the surrounding environment. These energy terms are not all independent, but are linked by the following relationships:

$$\frac{\delta Q_{s,out}}{dt} = -\frac{\delta Q_{w,in}}{dt} \quad (1a)$$

$$\frac{\delta Q_{w,out}}{dt} = -\frac{\delta Q_{h,in}}{dt} \quad (1b)$$

stating that the heat released by the particles is all transferred to the water in the eppendorf tube, and the heat in the eppendorf tube is all transferred to the quartz holder. The heat exchange is due to the temperature difference between the various constituents of the experimental setup and/or the surrounding environment. Therefore, the following equations can be written:

$$\frac{\delta Q_{s,out}}{dt} = -\frac{\delta Q_{w,in}}{dt} = -\frac{c_s m_s}{\tau_s} [T_s(t) - T_w(t)] \quad (2a)$$

$$\frac{\delta Q_{w,out}}{dt} = -\frac{\delta Q_{h,in}}{dt} = -\frac{(\alpha_{wh}\tau_{wh1} + (1 - \alpha_{wh})\tau_{wh2})c_w m_w}{\tau_{wh1}\tau_{wh2}} [T_w(t) - T_h(t)] \quad (2b)$$

$$\frac{\delta Q_{h,out}}{dt} = -\frac{(\alpha_{ha}\tau_{ha1} + (1 - \alpha_{ha})\tau_{ha2})c_h m_h}{\tau_{ha1}\tau_{ha2}} [T_h(t) - T_a(t)] \quad (2c)$$

where:

- c_s and m_s are the specific heat and mass, respectively, of the heat source (magnetic nanoparticles);
- τ_s is the time constant at which heat exchange from the source (nanoparticles) to the water contained in the eppendorf tube takes place;
- T_s is the time-varying temperature of the source (nanoparticles);
- T_w is the time-varying temperature of the water in the eppendorf tube;
- similarly, c_w and m_w are the specific heat and mass of the water in the eppendorf tube;
- τ_{wh1} and τ_{wh2} represent the time constants of the heat exchange mechanisms between the water in the eppendorf tube and the water filled quartz holder; two time constants are used as the experimental data indicate that two heat exchange mechanisms acting in parallel should be taken into account to reproduce the experiment; as they may not be equally efficient, a coefficient $\alpha_{wh} \in [0, 1]$ weights one mechanism with respect to the other; more details on how these time constants are obtained will be given later.;

- T_h is the time-varying temperature of the water in the quartz holder;
- c_h and m_h are the specific heat and mass of the water in the quartz holder (region surrounding the eppendorf tube);
- τ_{ha1} and τ_{ha2} represent the two time constants of the heat exchange mechanisms between the quartz holder and the outside ambient, weighted with their respective α_{ha} coefficient;
- T_a is the outside ambient temperature, that is assumed time-varying as the room temperature may be subject to drifts during the hyperthermia measurements.

Finally, the source term, that releases heat to the water contained in the eppendorf tube, must also directly include the power P_s provided by the electromagnetic field that excites the magnetic nanoparticles. Therefore, equation 2a should be replaced by:

$$\frac{\delta Q_s}{dt} = P_s - \frac{c_s m_s}{\tau_s} [T_s(t) - T_w(t)] \quad (3)$$

From the first principle of thermodynamics, $\Delta U = \Delta Q - \Delta L$ and by assuming $\Delta L = 0$ (i.e. there is no work against the outside, or the volume of the water contained in the eppendorf tube and in the quartz holder does not change with temperature, that is approximately true for temperature variations of just a few degrees), the overall heat change ΔQ in the system equals the variation of its internal energy ΔU , that is a function of its temperature. We can then write for the source, water in eppendorf and water in quartz holder terms respectively:

$$\frac{\Delta Q_{s,w,h}}{\Delta T_{s,w,h}} = c_{s,w,h} m_{s,w,h} \quad (4)$$

By combining equations 2, 3 and 4 one obtains:

$$c_s m_s \frac{dT_s(t)}{dt} = P_s - \frac{c_s m_s}{\tau_s} [T_s(t) - T_w(t)] \quad (5a)$$

$$c_w m_w \frac{dT_w(t)}{dt} = \frac{c_s m_s}{\tau_s} [T_s(t) - T_w(t)] - \frac{\alpha_{wh} \tau_{wh1} + (1 - \alpha_{wh}) \tau_{wh2}}{\tau_{wh1} \tau_{wh2}} c_w m_w [T_w(t) - T_h(t)] \quad (5b)$$

$$c_h m_h \frac{dT_h(t)}{dt} = \frac{\alpha_{wh} \tau_{wh1} + (1 - \alpha_{wh}) \tau_{wh2}}{\tau_{wh1} \tau_{wh2}} c_w m_w [T_w(t) - T_h(t)] + \frac{-\alpha_{ha} \tau_{ha1} + (1 - \alpha_{ha}) \tau_{ha2}}{\tau_{ha1} \tau_{ha2}} c_h m_h [T_h(t) - T_a(t)] \quad (5c)$$

Indeed, equations 5 omit an important contribution, that of the water contained in the eppendorf tube (even without the magnetic nanoparticles) and in the quartz holder, that subjected to the rf electromagnetic field heats up slightly due to ionic currents. Therefore, two power terms P_w and P_h must be added to equations 5 taking into account this effect. Additionally, when no particles are dispersed in the eppendorf tube (and therefore $P_s = 0$), the temperature of the water in the eppendorf tube and in the quartz tube must be the same ($T_w(t) = T_h(t)$), thus leading to a proportionality between P_w and P_h through the respective amounts of water: $P_h = \frac{m_h}{m_w} P_w$. As a consequence, the final equations describing the heat exchange between the various components of the hyperthermia setup and taking into account the heat dissipation towards the external environment and the heat released by the magnetic nanoparticles and by the ionic currents in the water when the rf electromagnetic field is on are the following:

$$c_s m_s \frac{dT_s(t)}{dt} = P_s - \frac{c_s m_s}{\tau_s} [T_s(t) - T_w(t)] \quad (6a)$$

$$c_w m_w \frac{dT_w(t)}{dt} = \frac{c_s m_s}{\tau_s} [T_s(t) - T_w(t)] + P_w - \frac{\alpha_{wh} \tau_{wh1} + (1 - \alpha_{wh}) \tau_{wh2}}{\tau_{wh1} \tau_{wh2}} c_w m_w [T_w(t) - T_h(t)] \quad (6b)$$

$$c_h m_h \frac{dT_h(t)}{dt} = \frac{\alpha_{wh} \tau_{wh1} + (1 - \alpha_{wh}) \tau_{wh2}}{\tau_{wh1} \tau_{wh2}} c_w m_w [T_w(t) - T_h(t)] + \frac{m_h}{m_w} P_w + \frac{-\alpha_{ha} \tau_{ha1} + (1 - \alpha_{ha}) \tau_{ha2}}{\tau_{ha1} \tau_{ha2}} c_h m_h [T_h(t) - T_a(t)] \quad (6c)$$

When the rf field is off, the same equations hold, but the two power terms P_s and P_w are equal to zero.

The three coupled differential equations (equations 6) can be solved (numerically) in the three unknowns $T_s(t)$, $T_w(t)$ and $T_h(t)$, of which:

- T_s is the temperature of the magnetic nanoparticles, and is not directly accessible; however, the model can estimate it, provided reasonable values for m_s , c_s and τ_s can be given (m_s being the only easily measurable quantity among these);
- T_w is the temperature of the water in the eppendorf, and is the quantity that is directly measured by the fiber optic thermometer;
- T_h is the temperature of the water in the quartz holder, and could be directly measured by the same thermometer if required.

In order to solve equations 6, the quantities listed in Table II must be known. Of these, $c_w = c_h$ are known from literature, m_w and m_h are known by design of the experimental setup, and m_s is measured when preparing each sample for hyperthermia characterization. The time coefficients τ_{wh1} , τ_{wh2} , τ_{ha1} and τ_{ha2} and the coefficients α_{wh} and α_{ha} are determined during system's calibration, as we will see shortly, as well as the power P_w released by the water submitted to the rf exciting field. c_s and τ_s are more difficult to be known, however their exact value is not strictly required for the determination of the specific absorption rate. In fact, c_s only affects the value of T_s obtained by solving equations 6, whereas the other two unknowns T_w (which is measured) and T_h remain unchanged. Since the temperature of the source (nanoparticles) is not directly measurable, a very precise value for c_s is not really required: a lower specific heat would result in nanoparticles having a higher temperature, and a higher specific heat would result in nanoparticles having a lower temperature, but the effect on the rest of the system, and especially on the temperature of the water solution T_w remains the same. For this reason, the value of c_s reported in literature for bulk Fe_3O_4 has been used; attempts to investigate the effect of particles size on the specific heat value, or to adapt it to different nanoparticles compositions, are out of the scope of this work. On the contrary, τ_s affects the speed at which the particles respond to the application of the rf field. Experimentally, the temperature of the water solution as measured by the fiber optic thermometer starts to increase almost immediately after the rf field is switched on; this

parameter	value	notes
c_s	$670 \text{ J kg}^{-1} \text{ K}^{-1}$	conventional value, affects T_s which cannot be directly measured
m_s	(...) mg	mass of particles, to be measured for each sample
τ_s	10 s	conventional value, must be $\ll \tau_{wh}$ and τ_{ha} to reproduce experimental data
P_s	(...) W	obtained iteratively by solving equations 6 and comparing T_w with the experimental data
c_w	$4187 \text{ J kg}^{-1} \text{ K}^{-1}$	specific heat of water
m_w	1 g	mass of water in eppendorf tube
τ_{wh1}	52.7 s	determined during system's calibration
τ_{wh2}	722.9 s	determined during system's calibration
α_{wh}	0.86	determined during system's calibration
c_h	$4187 \text{ J kg}^{-1} \text{ K}^{-1}$	specific heat of water
m_h	12 mg	mass of water in quartz holder inside rf coil volume
τ_{ha1}	800.1 s	determined during system's calibration
τ_{ha2}	9121.8 s	determined during system's calibration
α_{ha}	0.36 for $H_v = 30 \text{ mT}$ 0.60 for $H_v = 40 \text{ mT}$ 0.78 for $H_v = 50 \text{ mT}$ 0.76 for $H_v = 60 \text{ mT}$	determined during system's calibration
P_w	4.5 mW for $H_v = 30 \text{ mT}$ 11.5 mW for $H_v = 40 \text{ mT}$ 19.0 mW for $H_v = 50 \text{ mT}$ 26.5 mW for $H_v = 60 \text{ mT}$	determined during system's calibration

TABLE II. Values of the parameters appearing in equations 6.

suggests that the heating process begins immediately. Any value of τ_s would satisfactorily reproduce the experimental data, as long as τ_s is shorter than the time constants of the other heat exchange mechanisms. Finally, once the calibration and characterization of the experimental setup is complete, P_s remains as the only unknown parameter, which can be set arbitrarily and iteratively refined by comparing the time-dependent T_w value obtained by solving equations 6 with the experimental measurement of the temperature of the water solution. Once a satisfactory agreement is obtained between the experimental and calculated data, the value of P_s , divided by the particles mass m_s , gives the desired specific absorption rate.

In order to estimate the values of the parameters reported in Table II, a suitable calibra-

tion and characterization procedure of the experimental setup must be followed, that will be now detailed. The time constants τ_{wh1} and τ_{wh2} of the heat exchange mechanisms between the eppendorf tube and the water filled quartz holder, and their relative weight coefficient α_{wh} , can be obtained by putting in the eppendorf tube 1 mL of water (as 1 g is the chosen value for m_w) pre-heated at different temperatures (for example on a hot plate), in order to measure the time-evolution of the temperature of the water in the eppendorf as it cools down by exchanging heat with the surrounding water filled quartz holder. The time decay of the temperature, due to the difference between T_w (pre-heated externally) and T_h (at room temperature), can be measured with the fiber optics thermometer and subsequently fitted with the sum of two exponential functions. Figure 5 shows an example of the collected data, together with the fitting equation that has been used. This procedure has been repeated several times using water pre-heated at different temperatures, and the τ_{wh1} , τ_{wh2} and α_{wh} values averaged, giving the results reported in Table II. The data reported in Fig. 5 could not be fitted with a single exponential function, therefore two dissipations mechanisms with different time constants have been taken into account in the model leading to equations 6.

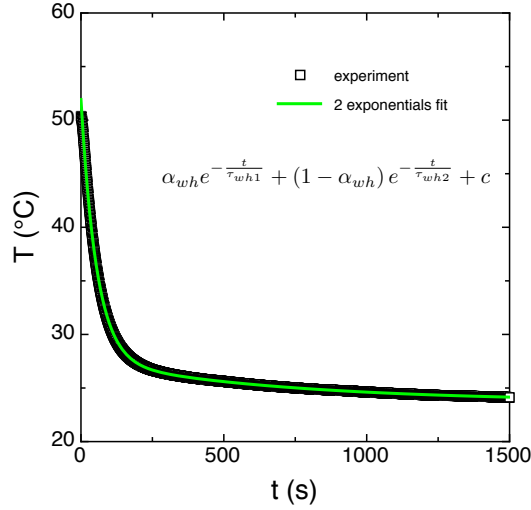


FIG. 5. Time decay of the temperature of the water contained in the eppendorf tube, without magnetic nanoparticles, pre-heated on a hot plate, and fitted with the sum of two exponentials.

To determine the time constants τ_{ha1} and τ_{ha2} and their relative weight coefficient α_{ha} , an eppendorf tube filled with 1 mL ($m_w = 1$ g) of water but without magnetic nanoparticles dispersed inside has been put in the water filled quartz holder. The rf field has been switched on at a given peak (or vertex) amplitude H_v , and the temperature T_w has been measured as

a function of time. After 1 h, the rf field has been switched off and T_w recorded for another hour while the system was cooling down. Then, equations 6 have been solved (using the τ_{wh1} , τ_{wh2} and α_{wh} values determined earlier and by putting $P_s = 0$), under the assumption, already discussed, that the temperature of the water in the eppendorf tube and in the quartz holder is the same (i.e. $T_w = T_h$ at any time). Four parameters must be iteratively varied in order to reproduce the experimental data: τ_{ha1} , τ_{ha2} and α_{ha} that affect the temperature dependence of T_w , and P_w that only affects how much the temperature of the water in the eppendorf tube increases (i.e. it simply scales the vertical axis of the calculated curve). An example for a H_v peak value of 50 mT is reported in Fig. 6. Several repetitions have been made for different H_v values from 30 to 60 mT. A weak, linear dependence of T_a over time has been considered when required to account for the variation of the temperature of the room during the measurements as time passed by. The values of τ_{ha1} , τ_{ha2} , α_{ha} and P_w obtained for the different H_v vertex values have then been averaged, and are reported in Table II.

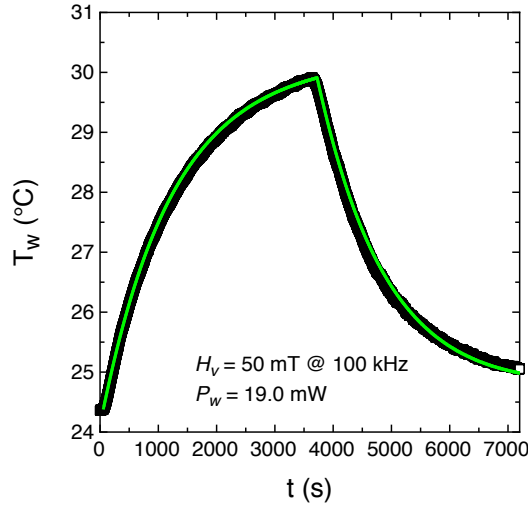


FIG. 6. Temperature dependence of the water in the eppendorf tube T_w (symbols) under an rf field H_v having a peak value of 50 mT. The power released by the water P_w as calculated by solving equations 6 (green line) is equal to 19 mW.

Once the hyperthermia setup characterization is complete, it can be used to measure the specific absorption rate of the desired water dispersion of magnetic nanoparticles. As an example, Fig. 7 shows the time-dependent variation of T_w for a solution containing 25 mg/mL of powders of sample Zn2, together with solution of equations 6 obtained for a value

of P_s equal to 700 mW, under an applied rf field of 30 mT. It is worth reminding that in order to solve equations 6 reported in Fig. 7 only one quantity (P_s) is unknown, all the others having been determined during the calibration process. Since the heat released by the water alone under a given rf field has been obtained as part of the calibration process and is properly taken into account in equations 6, P_s , which is adjusted iteratively, represents the actual power released by the source (magnetic nanoparticles). Divided by the mass of the particles, P_s gives the specific absorption rate:

$$SAR = \frac{P_s}{m_s} \quad (7)$$

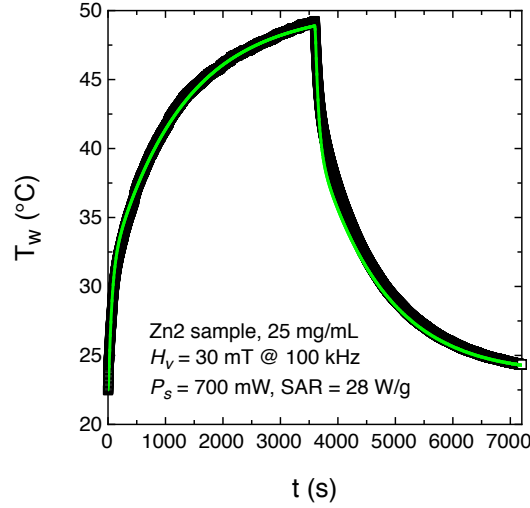


FIG. 7. Temperature dependence of the water dispersion of 25 mg/mL of powders of sample Zn2 in the eppendorf tube (T_w , symbols) under an rf field $H_v = 30$ mT. The power released by the particles P_s is calculated by solving equations 6 (green line) and is equal to 700 mW.

II.3. Hysteresis loops measurements

Magnetic hyperthermia exploits the frequency dependence of the complex magnetic permeability $\mu(\nu)$ of magnetic particles. The real part of the permeability enhances the response of the material to the magnetic field, whereas its imaginary part is responsible for the hysteresis losses, which cause energy dissipation in the material and, eventually, its heating. In order to investigate the mechanisms leading to the highest efficiency for hyperthermia applications and to optimize the materials' performance, it is of utmost importance to measure

hysteresis losses in magnetic nanoparticles, under experimental conditions as close as possible to those exploited in hyperthermia treatments. In particular, both vertex values of the applied field and field frequency should be chosen close to the ones used in the hyperthermia setups.

This requirement is particularly burdensome. The magnetometers normally used for the characterization of magnetic particles (e.g. VSM, SQUID) [46, 47] can apply very large fields, but only perform static measurements; at most, they can measure AC magnetic susceptibility at frequencies usually below 1 kHz and with maximum applied alternating fields of fractions of mT. Conversely, B-H loop tracers based on the inductive technique are able to measure frequency-dependent hysteresis loops (for applied field frequencies usually going up to a few hundred kHz or even a few MHz) [48], but the applied fields are extremely weak and cannot reach several tens of mT at frequencies of the order of 100 kHz (as for our hyperthermia setup). However, provided that hysteresis loops are available for the studied magnetic particles, their specific absorption rate can be estimated from the loops areas, that express the energy dissipated by the particles in one loop. It would therefore be extremely important to compare SAR values obtained from magnetic measurements with those measured in a hyperthermia setup.

To accomplish this task, we have used two different approaches. Static hysteresis loops have been measured on the studied samples, in dried form (i.e. the particles are not dispersed in water), by means of a vibrating sample magnetometer (VSM). Loops have been measured both at the maximum field that could be applied (1800 mT), and at vertex fields in the range 10 – 100 mT (i.e. the typical values in hyperthermia experiments), in static conditions. The magnetic moment measured by the VSM is normalized at the sample mass, then the loop area is calculated and converted to J/g. Finally, if we assume that the static hysteresis loop would remain unaltered if performed under a time-varying magnetic field at a frequency ν (e.g. $\nu = 100$ kHz as in our hyperthermia setup), the loop area can be multiplied by ν to obtain the power loss per unit mass, i.e. in W/g, as an estimate of the specific absorption rate of the magnetic nanoparticles.

Dynamic loops have instead been measured with a custom-built B-H loop tracer [49], whose schematic representation is given in Fig. 8.

A water-cooled copper pipe wound to form a coil is connected to the same power supply used for hyperthermia measurements. In order to accommodate the bulkier setup (compared

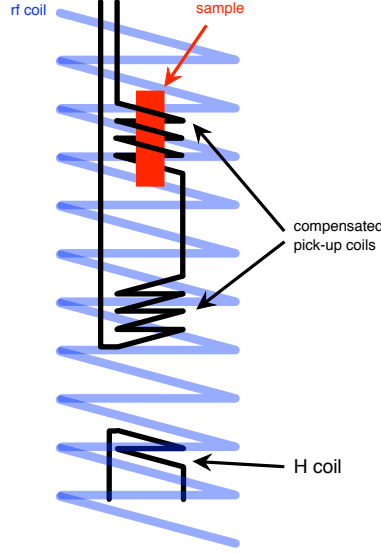


FIG. 8. Schematic representation of the B-H loop tracer used for dynamic hysteresis loops measurements.

to the hyperthermia one), a longer coil has been used; since the power supply operates in resonant conditions, the increased inductance reduces the actual rf field frequency to ≈ 69 kHz, which is still comparable to the 100 kHz of the exciting field used in hyperthermia experiments. In normal B-H loop tracers [50], the magnetic field is calculated from the measurement of the time-dependent electrical current that flows in the solenoid generating the field, once its calibration factor has been determined. However, in our setup, the high power required for operating the rf coil at such high frequency and field intensity prevents putting a resistor in series with the rf coil and measuring with an oscilloscope the time evolution of the current. Therefore, a field (H) pick-up coil, operating as a tensiometer, and having 2 turns, has been inserted in the rf exciting coil, and it has been calibrated to determine its cross section.

Similarly, in the rf exciting coil counter-wound B pick-up coils have been put, made of 10 turns and with a calibrated cross-section, that have been precisely built to compensate the concatenated flux, so that when no sample is inserted in one of the two coils, the induced voltage is equal to zero. Once a sample is inserted in one of the coil, the resulting unbalance induces an electromotive force at the two connectors of the B coils that is proportional to the time derivative of the sample magnetic induction. Both signals of the H and B coils are filtered with low noise pre-amplifiers (gain = 1, band pass from 10 to 300 kHz) and then

acquired with a digital oscilloscope. In order to take into account the parasitic capacitance of the twisted wires connecting both sets of coils to the amplifiers, a phase shift measurement has been performed with a lock-in amplifier between each of the two B coils and the H coil, and the resulting phase shifts subtracted. Then, the remaining parasitic phase shift is compensated during data analysis by offsetting the time base of the B signal with respect to the H signal by the proper angle. To obtain the final hysteresis loop, both H and B traces are downloaded from the oscilloscope, integrated, and the relevant calibrations applied in order to obtain H in T (or in A/m) and B in T. Then, the area of a single loop is calculated. Given the sample volume and mass, and the frequency of the rf field being known, the loop area in W/g can be calculated, equivalent to a dynamic magnetic measurement of the specific absorption rate.

It is worth commenting in more details the physical differences of the SAR values obtained by the three discussed techniques: static hysteresis loops, dynamic hysteresis loops and hyperthermia measurements. Static hysteresis loops only take into account the hysteresis losses arising from the magnetic anisotropy of the sample, either due to its crystalline microstructure or to local defects and imperfections. As static loops are measured in equilibrium conditions, no contribution due to Eddy currents is expected, neither at the scale of the sample volume (dynamic losses), nor at the scale of the domain walls or particles boundaries (excess losses) [51]. In general, SAR values obtained from static hysteresis loops are expected to underestimate SAR values in actual hyperthermia experiments, on the same samples.

Dynamic loops, on the contrary, exploit time-varying magnetic fields that can induce both dynamic and excess losses in the samples. The SAR values obtained by dynamic loops are expected to be higher than those measured by static loops, but depend on the measurement frequency, as both dynamic and excess losses depend on ν [51]. In our case, the small difference in operating frequency between the B-H loop tracer (≈ 69 kHz) and the hyperthermia setup (≈ 100 kHz) is expected to cause a small underestimate of the SAR value obtained by dynamic loops.

Hyperthermia experiments, finally, can provide a way to measure the specific absorption rate in conditions that usually do not match those available in VSM or SQUID systems and in B-H loop tracers: in fact, the magnetic particles are dispersed in solution for hyperthermia characterizations, but usually are not when hysteresis loops are measured. The mobility of

the particles in the solution during hyperthermia treatment may affect the heat dissipation mechanisms, by adding a friction contribution due to particles rotation in water, and by potentially reducing a magnetization reversal mechanism in the particles if they are able to follow to a certain extent the time-varying magnetic field by rotating under its influence. These contributions are not accessible by static loops measurements, but could be evaluated exploiting dynamic loops characterizations of water dispersed particles. However, the addition of water in the sample holder in a B-H loop tracer lowers the signal (as fewer particles are used) and adds a parasitic parallel capacitance to the pick-up coils, that is rather difficult to compensate [2], and may lead to unreliable measurements of B and therefore of loop area and SAR. In addition, the magnetic properties of particles dispersed in fluid may be significantly affected by their aggregation state, thus leading to even greater discrepancy between the SAR estimates obtained by static loops, dynamic loops and hyperthermia measurements [52, 53].

In the next section, static loops, dynamic loops and hyperthermia results will be compared on all samples listed in Table I.

III. RESULTS AND DISCUSSION

Two examples of hyperthermia characterizations of samples P1 and P2 are reported in Fig. 9. A full set of experimental T_w vs. t curves has been measured on both samples for different rf magnetic field intensities in the 30 – 60 mT range. The experimental curves have been compared with the calculated solutions of equations 6, until a satisfactory agreement has been found. The corresponding P_s value has then been used to calculate the SAR by means of equation 7. SAR values as a function of the rf magnetic field intensity are reported in Fig. 9 as well.

The hyperthermia behaviour of samples P1 and P2 is very different: P1 is characterized by a low SAR value that is constant with the applied field intensity, whereas sample P2 shows much larger SAR values, that increase with the rf applied field. At first, this behaviour seems in agreement with the static hysteresis loops of these two samples, discussed in Fig. 1: sample P1 is superparamagnetic, therefore having zero or at least negligible hysteresis losses. As a consequence, its SAR value is expected to be extremely low. Conversely, sample P2 is made of larger particles, that at room temperature have overcome their blocking temperature

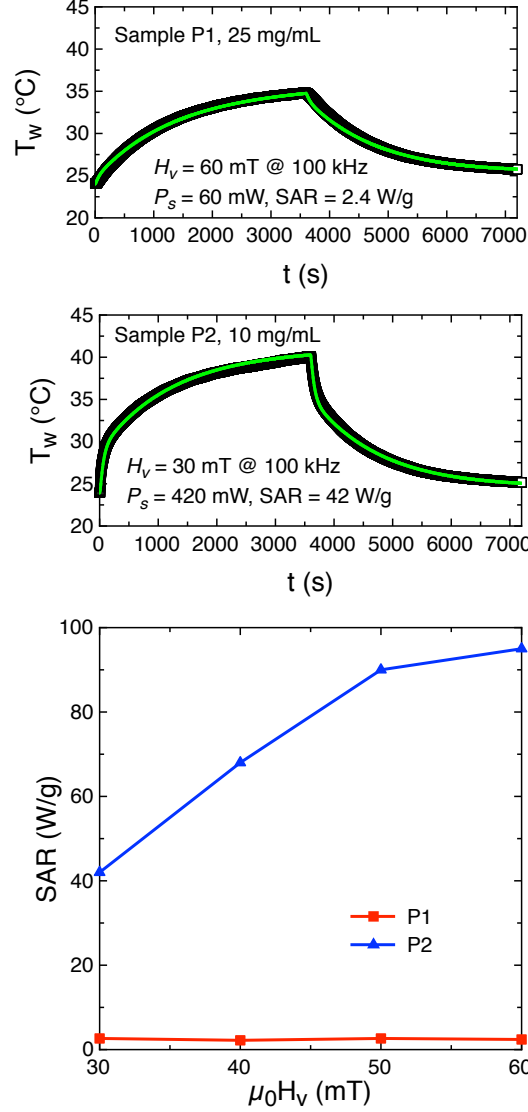


FIG. 9. Time dependence of the temperature T_w of the water solution containing P1 (top layer) or P2 (middle layer) particles at selected concentrations and applied rf fields: full symbols are the experimental data, green lines are the solutions of equations 6 for the indicated P_s value. Bottom layer: SAR dependence on the rf magnetic field intensity for samples P1 and P2.

and consequently present a magnetic hysteresis. As a result, a non negligible SAR value is obtained. However, this picture turns out to be somewhat too simplified.

Static and dynamic hysteresis loops have been measured on P1 and P2 particles in dried form at different maximum applied field values comparable to rf fields used in hyperthermia experiments. The results are summarized in Fig. 10. Static loops of sample P1 are not shown as all magnetization curves, acquired at different applied fields, perfectly superimpose, being

this sample superparamagnetic. Conversely, sample P2 shows a well defined increase of the static loop area as the maximum value of the applied field is increased. However, both samples report measurable loop areas when dynamic hysteresis loops are measured. Sample P2 continues displaying a larger hysteresis, while P1 presents a weaker but not negligible dependence on the maximum applied field value.

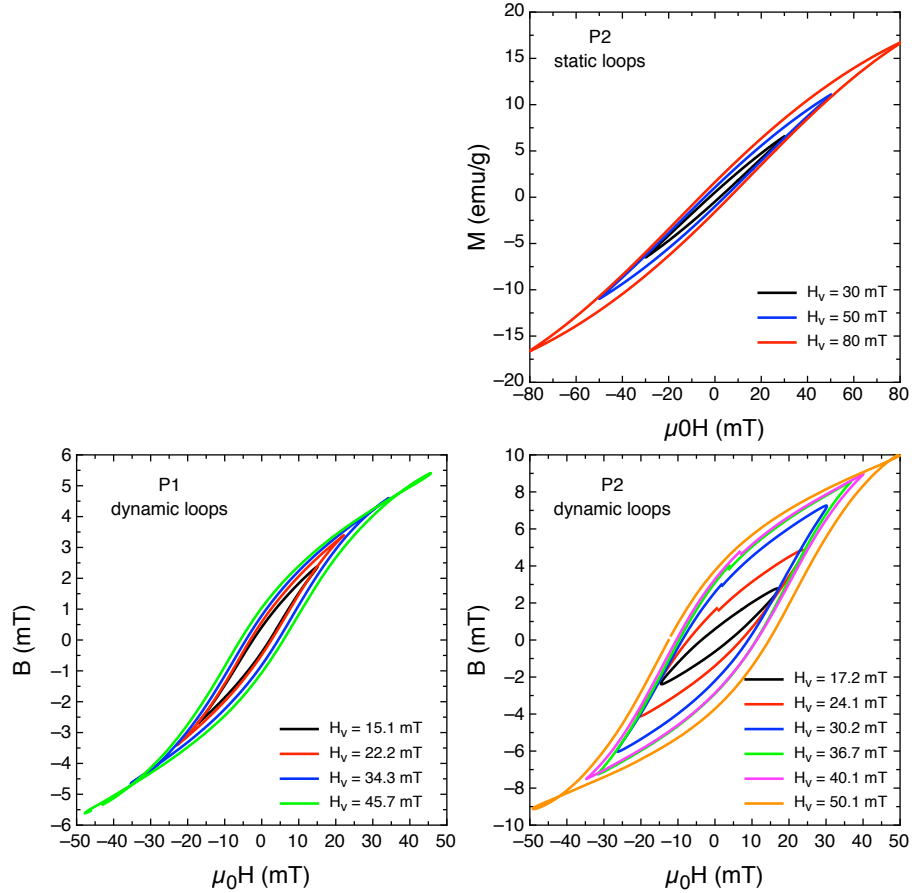


FIG. 10. Static and dynamic minor loops of samples P1 and P2 at room temperature at selected vertex fields.

A nanoparticles sample can be either in a superparamagnetic or blocked configuration [54] depending on the temperature at which it is measured, either above or below the so-called blocking temperature T_B , defined as:

$$T_B = \frac{KV}{\ln \frac{\tau}{\tau_0} k_B} \quad (8)$$

where K is the magnetic anisotropy of the particle, V its volume, k_B the Boltzmann constant, τ_0 is the characteristic Néel relaxation time (of the order of 10^{-9} s) and τ is the characteristic

time of the measurement performed on the particle. It is conventionally assumed that for static hysteresis loops measurements $\tilde{\tau} = 100$ s, and the logarithm is then approximately equal to 25. Given the material (e.g. Fe_3O_4 as is the case for samples P1 and P2), the blocking temperature increases if the particles size (and therefore their volume V) increases. It is therefore directly understandable why P1 is superparamagnetic and P2 is not, since P2 has larger particle sizes. Since T_B also depends on $\tilde{\tau}$, equation 8 also explains why the dynamic loops of sample P1 do not show a superparamagnetic behaviour: in fact, $\tilde{\tau}$ decreases from 100 s to $\approx 1.4 \cdot 10^{-5}$ s (the inverse of the rf field frequency of the B-H loop tracer), therefore by 7 orders of magnitude, therefore shifting T_B to much larger values.

However, when static or dynamic loops are measured, the samples are in dried form, therefore their particles tend to aggregate and constitute correlated magnetic units behaving as they were potentially much larger particles, potentially already in the blocked regime. When hyperthermia experiments are performed, instead, the particles are dispersed in water, where they interact with each other much more weakly and tend to form much smaller aggregates. This decreases the effective volume V of the particles in equation 8, therefore reducing T_B in hyperthermia measurements with respect to dynamic loops measurements. It is therefore possible that sample P2 is and remains ferromagnetic in all measurement conditions (static loops, dynamic loops, hyperthermia), whereas for sample P1 T_B crosses room temperature depending on the measurement conditions (superparamagnetic state during static loops, blocked state during dynamic loops because of decrease of $\tilde{\tau}$, superparamagnetic state during hyperthermia because of decrease of effective volume V), therefore leading to no static losses, measurable dynamic losses, but still a SAR value close to zero. It is also worth observing that the aggregates in quasi superparamagnetic systems, such as small nanoparticles dispersed in liquid as for sample P1, could have a SAR even lower than expected because of the possible effect of dipolar interactions on the Néel relaxation time, which lowers the efficiency of the energy absorption of the nanoparticles [52].

A summary of the SAR values determined with the three techniques for samples P1 and P2 is plotted in Fig. 11. As discussed above, sample P1 has a low and constant (with applied H_v value) SAR measured by hyperthermia, and low but increasing SAR values measured by dynamic loops areas. Static loop areas data are not reported as they are vanishing for this sample that is in a superparamagnetic condition. Conversely, sample P2 shows that the SAR determination by static loops areas is the lowest of the set. This is due to the

fact that static losses do not include all the dynamic contributions to the energy loss and therefore to the temperature increase of the material. In fact, SAR values calculated from dynamic loops areas turn out to be larger, even if SAR values obtained by hyperthermia measurements are even larger, partly because of the higher measurement frequency in the hyperthermia setup with respect to the B-H loop tracer, and possibly also indicating that in this sample energy loss mechanisms take place in the water dispersed particles that are not present in the dried sample used for hysteresis loops measurements. Indeed, the different aggregation states between the dried sample used for dynamic loops and the water solution used for hyperthermia may lead to different dipolar interactions within and among particles clusters, whose effects on SAR turn out to be complex and not easy to predict [53, 55].

Even though the specific absorption rate calculated from static hysteresis loops underestimates the actual power losses of magnetic particles in hyperthermia applications, it can be nonetheless a useful guide in selecting the most promising materials. An evidence is shown in Fig. 12, where areas of static hysteresis loops are reported for all studied Ni-Zn ferrites as a function of the maximum applied magnetic field H_v . The non-monotonous behaviour of their magnetic properties already discussed in Fig. 3 is visible here as well, with sample Zn2 displaying the largest static losses for $H_v \leq 60$ mT, even if this sample does not have the largest coercive field at saturation (see inset of Fig. 3). For comparison, Samples Zn2 (with the highest static losses) and Zn0 (with the lowest static losses) have been characterized by dynamic loops and hyperthermia measurements.

A selection of dynamic loops at different vertex fields H_v and a summary of the SAR estimates obtained with the three methods for Zn0 and Zn2 samples are reported in Fig. 13. As expected, the specific absorption rate determined by static losses is significantly underestimated, whereas for these samples dynamic losses and hyperthermia results overlap. This result can be attributed to at least two concurring causes. Even though the crystallites sizes reported in Table I are in the 20 – 30 nm range, ferrites prepared with sol-gel auto-combustion methods tend to sinter in quite large aggregates [56–59], that persist in the water solution. Therefore, the effective size of the elements whose magnetization is coherently excited by the rf field should remain approximately the same in both dynamic loops and hyperthermia experiments. In addition, the difference in the operating frequencies of the two setups does not induce significant variations of the magnetic losses because of the high resistivity of Ni-Zn ferrites (up to $10^9 \Omega\text{cm}$), especially when obtained with methods different

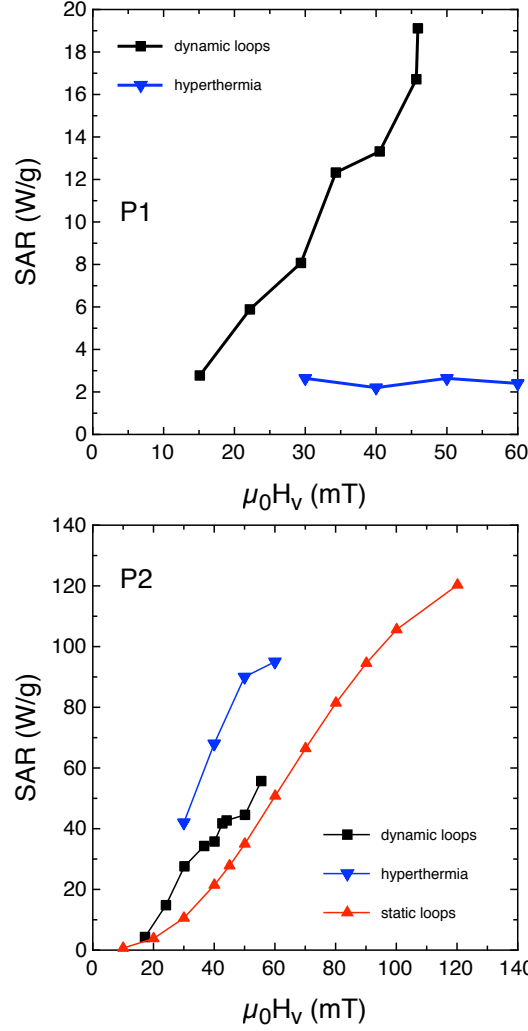


FIG. 11. SAR values for samples P1 and P2 as a function of the maximum applied magnetic field obtained by static hysteresis loops areas (red curves and upward triangles), dynamic loops areas (black curves and square symbols) and hyperthermia (blue curves and downward triangles).

than the conventional ceramic one, because of the relatively small crystallites sizes and well-defined grain boundaries [59–62]. In these conditions, the frequency dependence of the magnetic losses is reduced, and a remarkable overlap between the SAR values obtained by dynamic loops areas and hyperthermia measurements is obtained. With respect to the static loops measured at saturation (see Fig. 3), where sample Zn0 had the maximum coercivity and sample Zn2 the highest saturation, static loops measured at H_v values comparable to those of hyperthermia measurements correctly predict that the SAR for the Zn2 sample is higher than that of the Zn0 composition, even though for a correct measurement of the

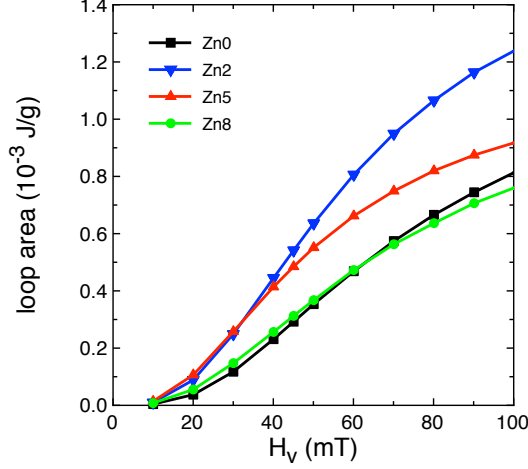


FIG. 12. Static hysteresis loops areas as a function of the maximum applied field for all studied Ni-Zn ferrites.

specific absorption rate either dynamic loops or hyperthermia experiments must be carried on.

IV. CONCLUSIONS

The necessity to assess the viability of magnetic nanoparticles hyperthermia as a therapeutic technique in tumor treatment requires the availability of experimental data regarding both the fundamental properties of the studied particles (magnetization curves, hysteresis losses) and their thermal properties during hyperthermia treatments. These data are often available from different sources in conditions that make them difficult to compare.

In this work, we have developed experimental techniques for determining the specific absorption rate of magnetic nanoparticles of interest for hyperthermia applications in three different ways: by evaluating static hysteresis loops areas, by evaluating dynamic hysteresis loops areas, and by measuring the temperature increase of a water solution containing the nanoparticles during exposition to a rf electromagnetic field. The first method is conventional and only requires commonly available magnetometers (such as VSM or SQUID), but has been shown to lead to SAR values that severely underestimate specific absorption rates in actual hyperthermia conditions. Moreover, in the case of superparamagnetic nanoparticles, both the magnetic interactions among them (that affect their effective volume) and the reduction by orders of magnitude of the measurement time (with respect to static loops) may lead

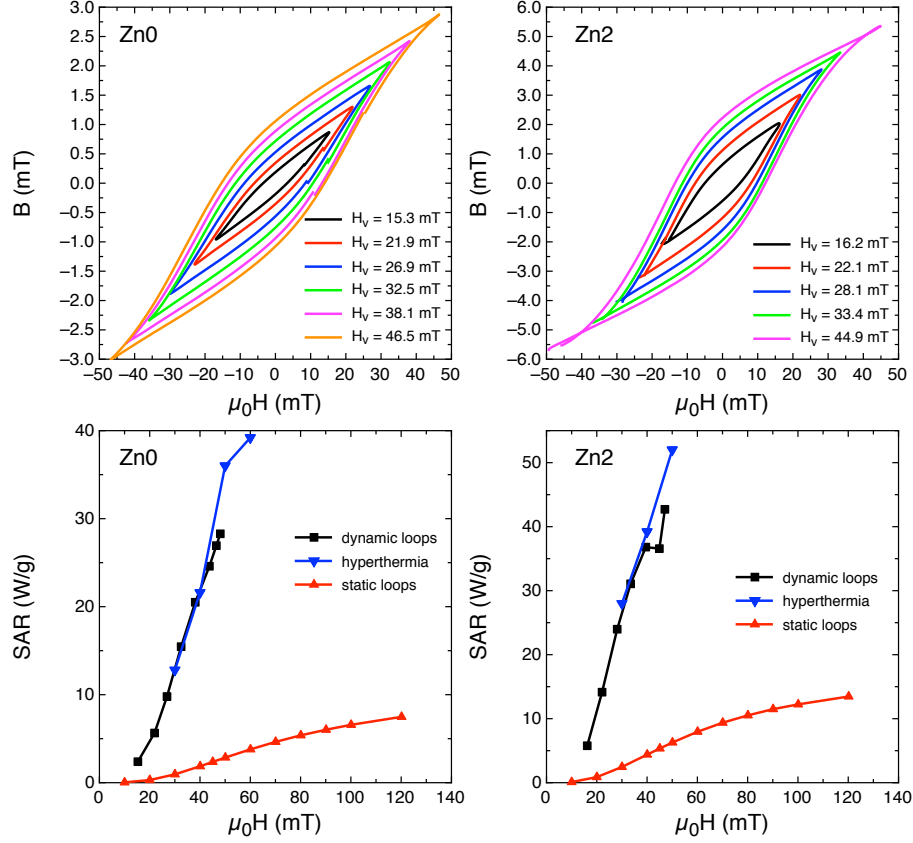


FIG. 13. Dynamic hysteresis loops at selected vertex fields and SAR measurements obtained with the three methods (static loops: red curves and upward triangles; dynamic loops: black curves and squares; hyperthermia: blue curves and downward triangles) on Zn0 and Zn2 Ni-Zn ferrite samples.

to significant variations of their blocking temperature, that could cross room temperature in hyperthermia conditions, whereas the nanoparticles still appear superparamagnetic when static loops are concerned. However, for ferromagnetic samples with a significant hysteresis, static loops provide nonetheless a valuable tool to select the candidate materials having the best expected SAR values through a careful analysis of the loops areas within the magnetic field values of interest for hyperthermia applications.

The second method, i.e. the measurement of dynamic loops at frequencies and magnetic field intensities comparable to hyperthermia conditions, cannot exploit conventional B-H loop tracers, as the power required to generate a magnetic component of the rf field up to several tens of mT at frequencies of the order of $\approx 10^5$ Hz is excessive. Therefore, we adapted the hyperthermia setup to measure dynamic hysteresis loops on magnetic nanoparticles, although in dried form. With respect to conventional B-H loop tracers, the main difference

is the measurement of the H component, that requires an additional tensiometer instead of a normal resistor in series with the coil or solenoid. After proper calibration of the cross sections of the H and B pick-up coils, dynamic loops on magnetic nanoparticles can be used to estimate SAR values where the dynamic components of the losses are not neglected.

The third method is a direct measurement of the specific absorption rate with a magnetic hyperthermia setup. The usual limitations of this kind of equipments (i.e. the necessity to assume adiabatic conditions and to perform, as a consequence, very short measurements, when only very limited temperature increases are reached) have been addressed by developing an experimental setup operating in non-adiabatic conditions, where the heat exchange of its components among themselves and with the surrounding environment have been properly taken into account in a thermodynamic model. A calibration procedure allows to determine all the physical quantities appearing in the mathematical model, leaving as a free parameter only the power released by the magnetic nanoparticles to the water solution, whose temperature is experimentally measured. By comparing the experimental data and the results of the integration of the model equations, the specific absorption rate of the particles can be reliably attained. Dynamic hysteresis losses have been also shown to correctly give hyperthermia SAR values in magnetic particles whose ferromagnetic behaviour is already sufficiently strong even in static loops measurements.

Finally, it should be noted that the thermodynamical model used for the hyperthermia setup is quite general and could be adapted to other systems as well. In addition, it could provide useful information on the thermal properties of the magnetic nanoparticles. In fact, if their specific heat is known with sufficient precision, the model is able to predict the actual temperature of the particles (and not only of the water solution containing them), that is normally not accessible, and that could be an important quantity to know for determining potentially harmful effects of hyperthermia on living tissues. Moreover, the model would even allow the determination of a temperature-dependent SAR, should self-limiting magnetic nanoparticles be employed [63–66]. In this case, in fact, SAR would not have a unique value any more, as the heat transfer efficiency of the particles would depend on their temperature (and its proximity with their Curie temperature), and all methods of SAR evaluation not based on the analysis of a whole time-dependent temperature curve would be inadequate. Instead, in the present model, a temperature dependence of P_s could be imposed, although to the detriment of an easy integration of the set of thermodynamical equations.

ACKNOWLEDGMENTS

The authors would like to thank Politronica s.r.l., in the persons of Dr. Paola Martino and Dr. Giuseppe Ferraro, for providing some of the samples. One author, S.R., acknowledges the support of UGC-DAE CSR, Indore project: CSR-IC/CRS-74/2014-15/2104.

REFERENCES

-
- [1] S. Dutz, R. Hergt, *Magnetic particle hyperthermia - a promising tumor therapy?*, Nanotechnology **25** (2014) 452001.
 - [2] A. Périgo, G. Hemery, O. Sandre, D. Ortega, E. Garaio, F. Palazola, F.J. Teran, *Fundamentals and advances in magnetic hyperthermia*, Appl. Phys. Rev. **2** (2015) 041302.
 - [3] M. Latorre, C. Rinaldi, *Applications of magnetic nanoparticles in medicine: magnetic fluid hyperthermia*, PRHSJ **28** (2009) 227.
 - [4] G. Vallejo-Fernandez, O. Whear, A.G. Roca, S. Hussain, J. Timmis, V. Patel, K. O'Grady, *Mechanisms of hyperthermia in magnetic nanoparticles*, J. Phys. D: Appl. Phys. **46** (2013) 312001.
 - [5] J. van der Zee, *Heating the patient: a promising approach?*, Ann. Oncol. **13** (2002) 1173.
 - [6] C. Blanco-Andujar, D. Ortega, P. Southern, S.A. Nesbitt, N.T.K. Thanh, Q.A. Pankhurst, *Real-time tracking of delayed-onset cellular apoptosis induced by intracellular magnetic hyperthermia*, Nanomedicine **11** (2016) 121.
 - [7] C.S. Kumar, F. Mohammad, *Magnetic nanomaterials for hyperthermia-based therapy and controlled drug delivery*, Adv. Drug. Delivery Rev. **63** (2011) 789.
 - [8] F. Cardoso, A. Costa, L. Norton, E. Senkus, M. Aapro, F. André, C.H. Barrios, J. Bergh, L. Biganzoli, K.L. Blackwell, M.J. Cardoso, T. Cufer, N. El Saghir, L. Fallowfield, D. Fenech, P. Francis, K. Gelmon, S.H. Giordano, J. Gligorov, A. Goldhirsch, N. Harbeck, N. Houssami, C. Hudis, B. Kaufman, I. Krop, S. Kyriakides, U.N. Lin, M. Mayer, S.D. Merjaver, E.B. Nordström, O. Pagani, A. Partridge, F. Penault-Llorca, M.J. Piccart, H. Rugo, G. Sledge, C. Thomssen, L. van't Veer, D. Vorobiof, C. Vrieling, N. West, B. Xu, E. Winer, *ESO-ESMO 2nd*

- international consensus guidelines for advanced breast cancer (ABC2)*, Ann. Oncol. (2014) 1.
- [9] R. Hergt, S. Dutz, R. Müller, M. Zeisberger, *Magnetic particle hyperthermia: nanoparticle magnetism and materials development for cancer therapy*, J. Phys.: Condens. Matter **18** (2006) S2919.
- [10] A.E. Deatsch, B.A. Evans, *Heating efficiency in magnetic nanoparticle hyperthermia*, J. Magn. Magn. Mater. **354** (2014) 163.
- [11] E. Natividad, M. Castro, A. Mediano, *Adiabatic vs. non-adiabatic determination of specific absorption rate of ferrofluids*, J. Magn. Magn. Mater. **321** (2009) 1497.
- [12] Nguyen T.K. Thanh (Ed.), *Magnetic Nanoparticles from Fabrication to Clinical Application*, CRC Press, Taylor & Francis Group, FL, USA, 2012.
- [13] A. Figuerola, R. Di Corato, L. Manna, T. Pellegrino, *From iron oxide nanoparticles towards advanced iron-based inorganic materials designed for biomedical applications*, Pharmacol. Res. **62** (2010) 126.
- [14] R. Di Corato, A. Espinosa, L. Lartigue, M. Tharaud, S. Chat, T. Pellegrino, C. Ménager, F. Gazeau, C. Wilhelm, *Magnetic hyperthermia efficiency in the cellular environment for different nanoparticle designs*, Biomaterials **35** (2014) 6400.
- [15] K. Simeonidis, C. Martinez-Boubeta, Ll. Balcells, C. Monty, G. Stavropoulos, M. Mitrakas, A. Matsakidou, G. Vourlias, M. Angelakeris, *Fe-based nanoparticles as tunable magnetic particle hyperthermia agents*, J. Appl. Phys. **114** (2013) 103904.
- [16] M. Filippousi, T. Altantzis, G. Stefanou, M. Betsiou, D.N. Bikiaris, M. Angelakeris, E. Pavlidou, D. Zamboulis, G. Van Tendeloo, *Polyhedral iron oxide core-shell nanoparticles in a biodegradable polymeric matrix: preparation, characterization and application in magnetic particle hyperthermia and drug delivery*, RSC Adv. **3** (2013) 24367.
- [17] X.L. Liu, Y. Yang, C.T. Ng, L.Y. Zhao, Y. Zhang, B.H. Bay, H.M. Fan, *Magnetic vortex nanorings: a new class of hyperthermia agent for highly efficient in vivo regression of tumors*, J. Ding, Adv. Mater. **27** (2015) 1939.
- [18] E.A. Rozhkova, V. Novosad, D.-H. Kim, J. Pearson, R. Divan, T. Rajh, S.D. Bader, *Ferro-magnetic microdisks as carriers for biomedical applications*, J. Appl. Phys. **105** (2009) 07B306.
- [19] D.-H. Kim, E.A. Rozhkova, I.V. Ulasov, S.D. Bader, T. Rajh, M.S. Lesniak, *Biofunctionalized magnetic-vortex microdiscs for targeted cancer-cell destruction*, V. Novosad, Nat. Mater. **9** (2010) 165.

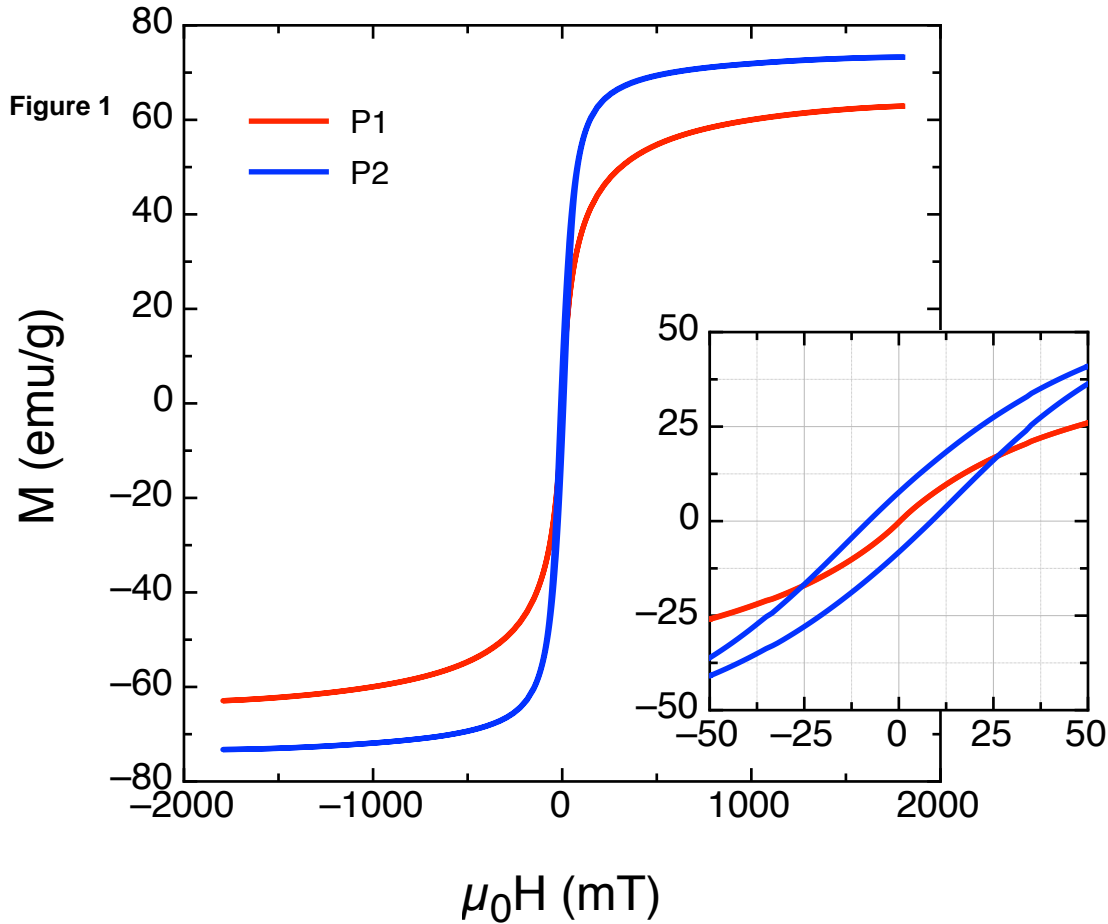
- [20] P. Tiberto, G. Barrera, F. Celegato, G. Conta, M. Coisson, F. Vinai, F. Albertini, *Ni₈₀Fe₂₀ nanodisks by nanosphere lithography for biomedical applications*, J. Appl. Phys. **117** (2015) 17B304.
- [21] F. Liu, Y. Hou, S. Gao, *Exchange-coupled nanocomposites: chemical synthesis, characterization and applications*, Chem. Soc. Rev. **43** (2014) 8098.
- [22] A. Espinosa, R. Di Corato, J. Kolosnjaj-Tabi, P. Flaud, T. Pellegrino, C. Wilhelm, *Duality of Iron Oxide Nanoparticles in Cancer Therapy: Amplification of Heating Efficiency by Magnetic Hyperthermia and Photothermal Bimodal Treatment*, ACS Nano **10** (2016) 2436.
- [23] D.H. Ortgies, L. de la Cueva, B. del Rosal, F. Sanz-Rodríguez, N. Fernández, M.C. Iglesias-de la Cruz, G. Salas, D. Cabrera, F.J. Teran, D. Jaque, E. Martín Rodríguez, *In Vivo Deep Tissue Fluorescence and Magnetic Imaging Employing Hybrid Nanostructures*, ACS Appl. Mater. Interf. **8** (2016) 1406.
- [24] A. Chalkidou, K. Simeonidis, M. Angelakeris, T. Samaras, C. Martinez-Boubeta, Ll. Balcells, K. Papazisis, C. Dendrinou-Samara, O. Kalogirou, *In vitro application of Fe/MgO nanoparticles as magnetically mediated hyperthermia agents for cancer treatment*, J. Magn. Magn. Mater. **323** (2011) 775.
- [25] M. Coisson, G. Barrera, F. Celegato, L. Martino, F. Vinai, P. Martino, G. Ferraro, P. Tiberto, *Specific absorption rate determination of magnetic nanoparticles through hyperthermia measurements in non-adiabatic conditions*, J. Magn. Magn. Mater. **415** (2016) 2.
- [26] E. Garaio, J.-M. Collantes, J.A. Garcia, F. Plazaola, O. Sandre, *Harmonic phases of the nanoparticle magnetization: An intrinsic temperature probe*, Appl. Phys. Lett. **107** (2015) 123103.
- [27] RADIOMAG COST action, August 2016 newsletter, http://www.cost-radiomag.eu/News/RADIOMAG-newsletter-August-issue_1
- [28] M. Panteghini, *Traceability as a unique tool to improve standardization in laboratory medicine*, Clinical Biochem. **42** (2009) 236.
- [29] M. Panteghini, J.C. Forest, *Standardization in laboratory medicine: New challenges*, Clinica Chimica Acta **355** (2005) 1.
- [30] M.M. Müller, *Implementation of Reference Systems in Laboratory Medicine*, Clinical Chemistry **46** (2000) 1907.

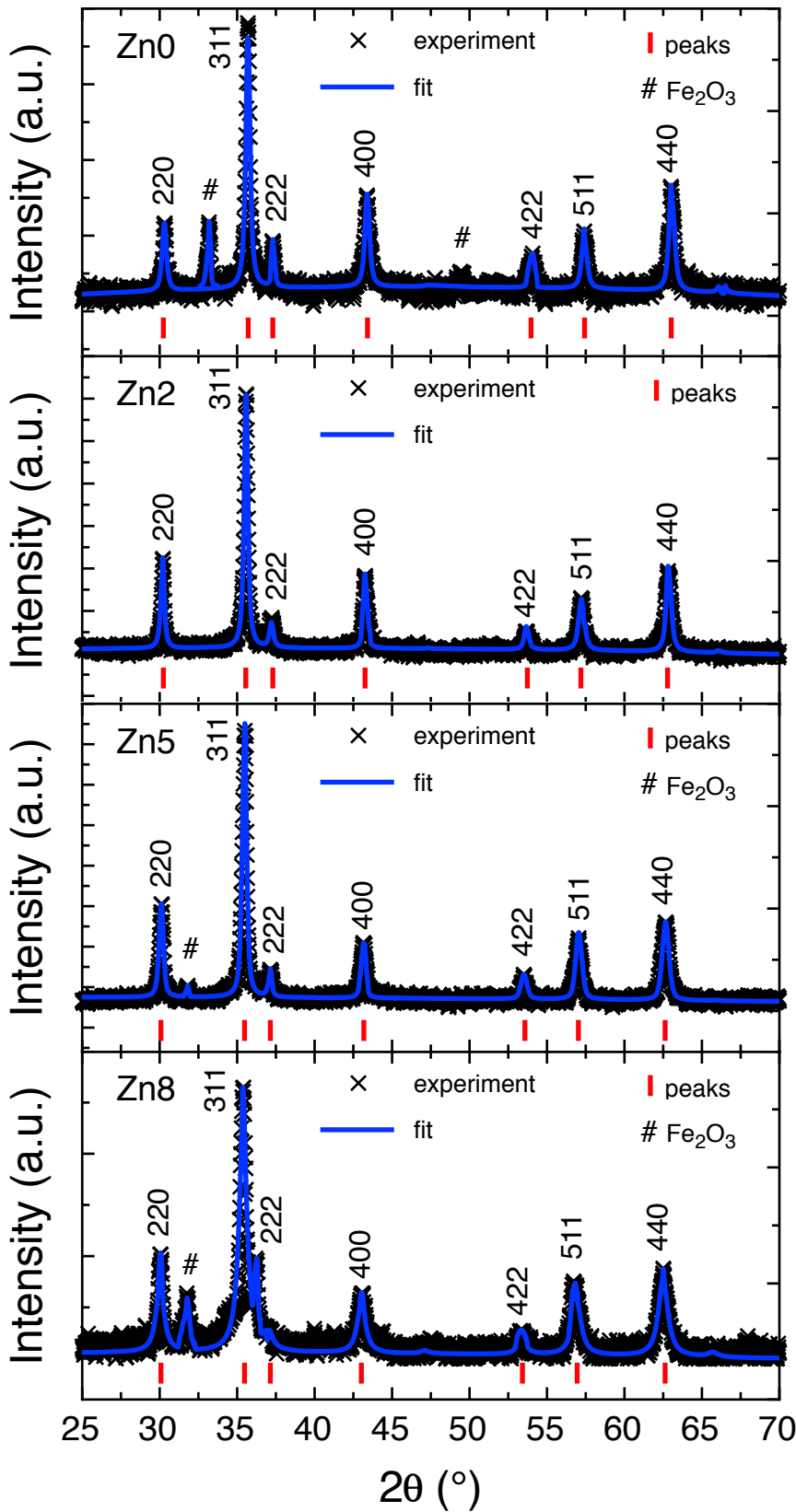
- [31] R. Chen, M.G. Christiansen, P. Anikeeva, *Maximizing Hysteretic Losses in Magnetic Ferrite Nanoparticles via Model-Driven Synthesis and Materials Optimization*, ACS Nano **7** (2013) 8990.
- [32] M. Vasilakaki, C. Binns, K.N. Trohidou, *Susceptibility losses in heating of magnetic core/shell nanoparticles for hyperthermia: a Monte Carlo study of shape and size effects*, Nanoscale **7** (2015) 7753.
- [33] R. Hergt, S. Dutz, M. Röder, *Effects of size distribution on hysteresis losses of magnetic nanoparticles for hyperthermia*, J. Phys.: Cond. Matter **20** (2008) 385214.
- [34] R. Hergt, R. Hiergeist, I. Hilger, W.A. Kaiser, Y. Lapatnikov, S. Margel, U. Richter, *Maghemite nanoparticles with very high AC-losses for application in RF-magnetic hyperthermia*, J. Magn. Magn. Mater. **270** (2004) 345.
- [35] A. Makridis, K. Topouridou, M. Tziomaki, D. Sakellari, K. Simeonidis, M. Angelakeris, M.P. Yavropoulou, J.G. Yovos, O. Kalogirou, *In vitro application of Mn-ferrite nanoparticles as novel magnetic hyperthermia agents*, J. Mater. Chem. B **2** (2014) 8390.
- [36] Y. Oh, N. Lee, H.W. Kang, J. Oh, *In vitro study on apoptotic cell death by effective magnetic hyperthermia with chitosan-coated $MnFe_2O_4$* , Nanotechnology **27** (2016) 115101.
- [37] I. Sharifi, H. Shokrollahi, S. Amiri, *Ferrite-based magnetic nanofluids used in hyperthermia applications*, J. Magn. Magn. Mater. **324** (2012) 903.
- [38] M. S. Al-Qubaisi, A. Rasedee, M.H. Flaifel, S.H.J. Ahmad, S. Hussein-Al-Ali, M.Z. Hussein, E.E.M. Eid, Z. Zainal, M. Saeed, M. Ilowefah, S. Fakurazi, N.M. Isa, M.E.E. Zowalaty, *Cytotoxicity of nickel zinc ferrite nanoparticles on cancer cells of epithelial origin*, Int. J. Nanomedicine **8** (2013) 2497.
- [39] M. Satalkar, S.N. Kane, A. Gosh, N. Ghodke, G. Barrera, F. Celegato, M. Coisson, P. Tiberto, F. Vinai, *Synthesis and soft magnetic properties of $Zn_{0.8-x}Ni_xMg_{0.1}Cu_{0.1}Fe_2O_4$ ($x = 0.0 - 0.8$) ferrites prepared by sol-gel auto-combustion method*, J. All. Comp. **615** (2014) S313.
- [40] L. Gastaldi, A. Lapicciarella, *Three different methods of determining the cation distribution in spinels: A comparison*, J. Solid State Chem. **30** (1979) 223.
- [41] C.M.B. Henderson, J.M. Charnock, D.A. Plant, *Cation occupancies in Mg, Co, Ni, Zn, Al ferrite spinels: a multi-element EXAFS study*, J. Phys.: Cond. Matter **19** (2007) 076214.
- [42] T.J. Shinde, A.B. Gadkari, P.N. Vasambekar, *Magnetic properties and cation distribution study of nanocrystalline Ni-Zn ferrites*, J. Magn. Magn. Mater. **333** (2013) 152.

- [43] R. Hergt, S. Dutz, M. Zeisberger, *Validity limits of the Néel relaxation model of magnetic nanoparticles for hyperthermia*, Nanotechnology **21** (2010) 015706.
- [44] E. Natividad, M. Castro, A. Mediano, *Accurate measurement of the specific absorption rate using a suitable adiabatic magnetothermal setup*, Appl. Phys. Lett. **92** (2008) 093116.
- [45] R.R. Wildeboer, P. Southern, Q.A. Pankhurst, *On the reliable measurement of specific absorption rates and intrinsic loss parameters in magnetic hyperthermia materials*, J. Phys. D: Appl. Phys. **47** (2014) 495003.
- [46] R.D. Zysler, D. Fiorani, A.M. Testa, *Investigation of magnetic properties of interacting Fe_2O_3 nanoparticles*, J. Magn. Magn. Mater. **224** (2001) 5.
- [47] P. Allia, G. Barrera, P. Tiberto, T. Nardi, Y. Leterrier, M. Sangermano, *Fe_3O_4 nanoparticles and nanocomposites with potential application in biomedicine and in communication technologies: Nanoparticle aggregation, interaction, and effective magnetic anisotropy*, J. Appl. Phys. **116** (2014) 113903.
- [48] F. Fiorillo, C. Beatrice, M. Coisson, L. Zhemchuzhna, *Loss and Permeability Dependence on Temperature in Soft Ferrites*, IEEE Trans. Magn. **45** (2009) 4242.
- [49] E. Garajo, J.M. Collantes, J.A. Garcia, F. Plazaola, S. Mornet, F. Couillaud, O. Sandre, A *wide-frequency range AC magnetometer to measure the specific absorption rate in nanoparticles for magnetic hyperthermia*, J. Magn. Magn. Mater. **368** (2014) 432.
- [50] F. Fiorillo, *Measurement and characterization of magnetic materials*, Isaak Mayergoyz editor, Elsevier (2004) San Diego (USA).
- [51] G. Bertotti, *Hysteresis in magnetism*, Academic Press (1998) San Diego (USA).
- [52] N. Iacob, G. Schinteie, C. Barthä, P. Palade, L. Vekas V. Kuncser, *Effects of magnetic dipolar interactions on the specific time constant in superparamagnetic nanoparticle systems*, J. Phys. D: Appl. Phys. **49** (2016) 295001.
- [53] J.C. Ovejero, D. Cabrera, J. Carrey, T. Valdivielso, G. Salas, F.J. Teran, *Effects of inter- and intra-aggregate magnetic dipolar interactions on the magnetic heating efficiency of iron oxide nanoparticles*, Phys. Chem. Chem. Phys. **18** (2016) 10954.
- [54] B.D. Cullity, C.D. Graham, *Introduction to magnetic materials*, Wiley (2009) Hoboken (USA).
- [55] P. de la Presa, Y. Luengo, V. Velasco, M.P. Morales, M. Iglesias, S. Veintemillas-Verdaguer, P. Crespo, A. Hernando, *Particle Interactions in Liquid Magnetic Colloids by Zero Field Cooled Measurements: Effects on Heating Efficiency*, J. Phys. Chem. C **119** (2015) 11022.

- [56] P. Sivakumar, R. Ramesh, A. Ramanand, C. Muthamizhchelvan, *Synthesis and characterization of nickel ferrite magnetic nanoparticles*, Mater. Res. Bulletin **46** (2011) 2208.
- [57] A. Sutka, G. Mezinskas, A. Pludons, S. Lagzdina, *Characterization of sol-gel auto-combustion derived spinel ferrite nano-materials*, Energetika **56** (2010) 254.
- [58] X. Zhang, Z. Hua, S. Yang, *Sol-gel autocombustion synthesis and characterization of $Fe_{1-x}Co_x$ alloys with large saturation magnetization*, Sol-Gel Sci. Technol. **78** (2016) 171.
- [59] A. Verma, T.C. Goel, R.G. Mendiratta, R.G. Gupta, *High-resistivity nickel-zinc ferrites by the citrate precursor method*, J. Magn. Magn. Mater. **192** (1999) 271.
- [60] T.J. Shinde, A.B. Gadkari, P.N. Vasambekar, *DC resistivity of Ni-Zn ferrites prepared by oxalate precipitation method*, Mater. Chem. Phys. **111** (2008) 87.
- [61] K. Rama Krishna, K. Vijaya Kumar, D. Ravinder, *Structural and Electrical Conductivity Studies in Nickel-Zinc Ferrite*, Adv. Mater. Phys. Chem. **2** (2012) 185.
- [62] M. Siva Ram Prasad, K.V. Ramesh, B. Rajesh Babu, K. Trinath, *DC electrical resistivity and dielectric properties of Ni-Zn nanoferrite synthesized via autocombustion route*, Indian J. Phys. **90** (2016) 417.
- [63] T.N. Brusentsova, N.A. Brusentsov, V.D. Kuznetsov, V.N. Nikiforov, *Synthesis and investigation of magnetic properties of Gd-substituted Mn-Zn ferrite nanoparticles as a potential low- T_C agent for magnetic fluid hyperthermia*, J. Magn. Magn. Mater. **293** (2005) 298.
- [64] K.L. McNerny, Y. Kim, D.E. Laughlin, M.E. McHenry, *Chemical synthesis of monodisperse γ -Fe-Ni magnetic nanoparticles with tunable Curie temperatures for self-regulated hyperthermia*, J. Appl. Phys. **107** (2010) 09A312.
- [65] E. Pollert, K. Knížek, M. Maryško, P. Kašpar, S. Vasseur, E. Duguet, *New T_C -tuned magnetic nanoparticles for self-controlled hyperthermia*, J. Magn. Magn. Mater. **316** (2007) 122.
- [66] J. Chatterjee, M. Bettge, Y. Haik, C.J. Chen, *Synthesis and characterization of polymer encapsulated Cu-Ni magnetic nanoparticles for hyperthermia applications*, J. Magn. Magn. Mater. **293** (2005) 303.

Figure 1





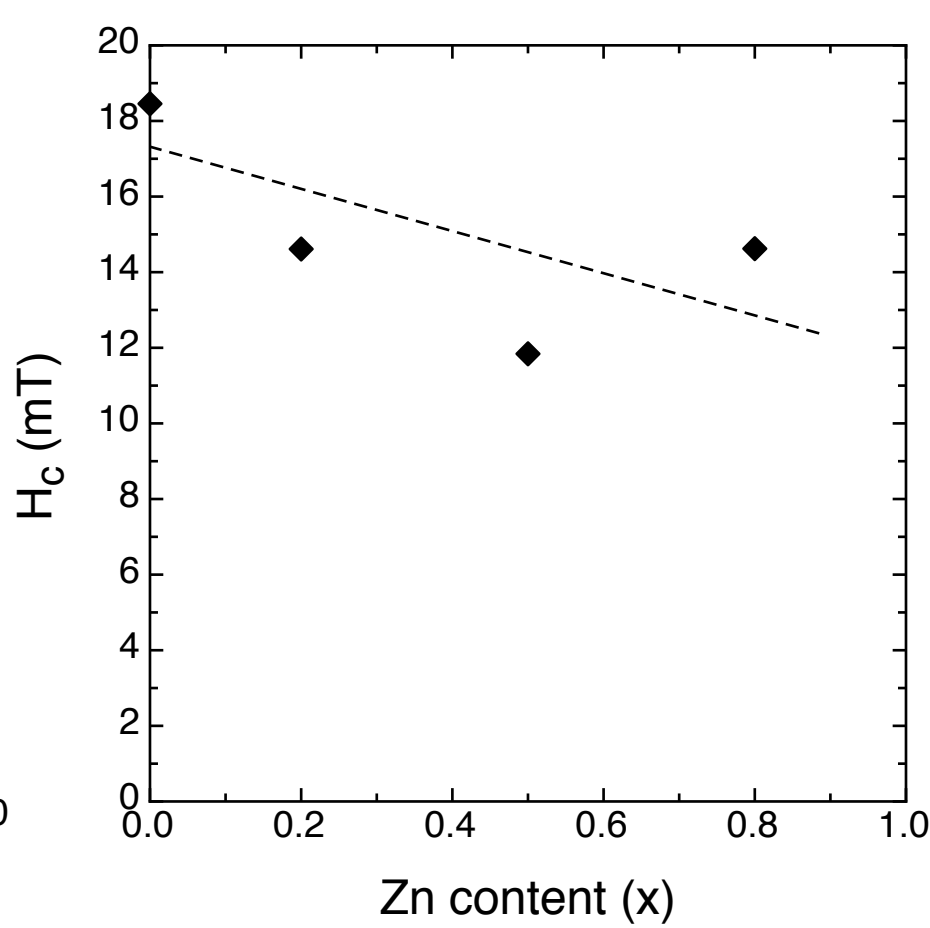
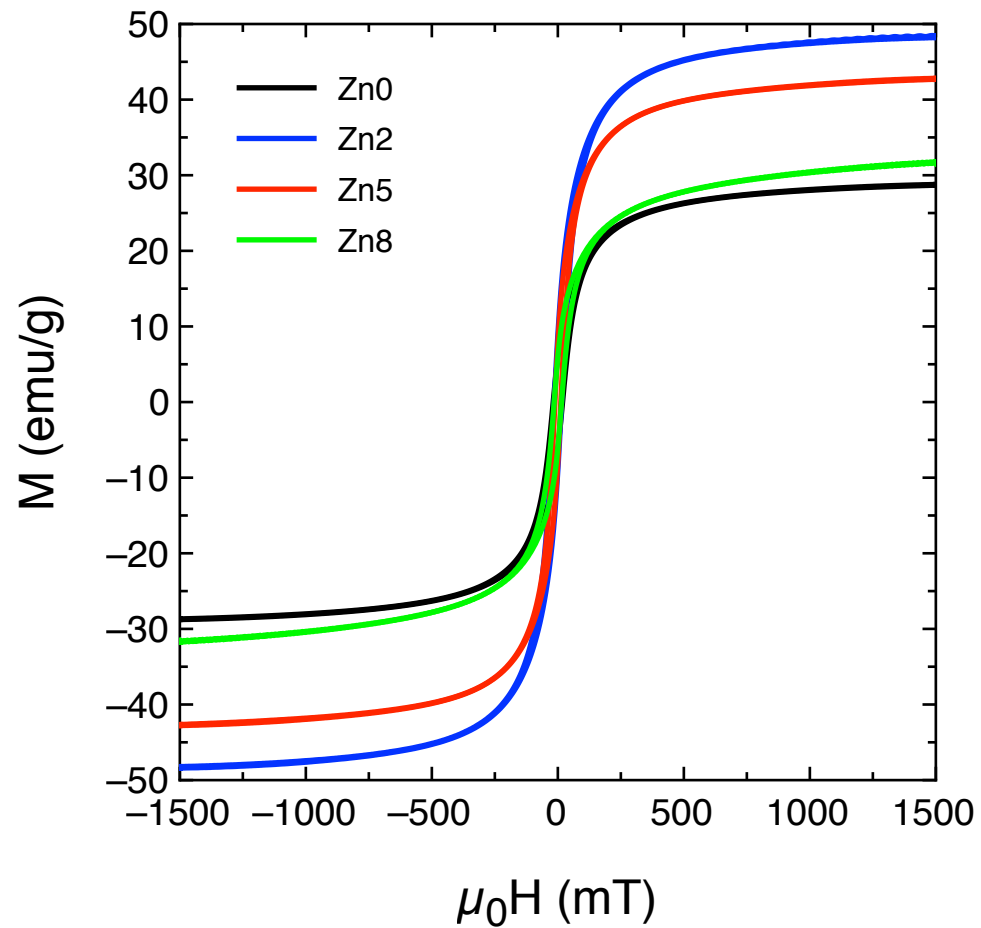


Figure 4

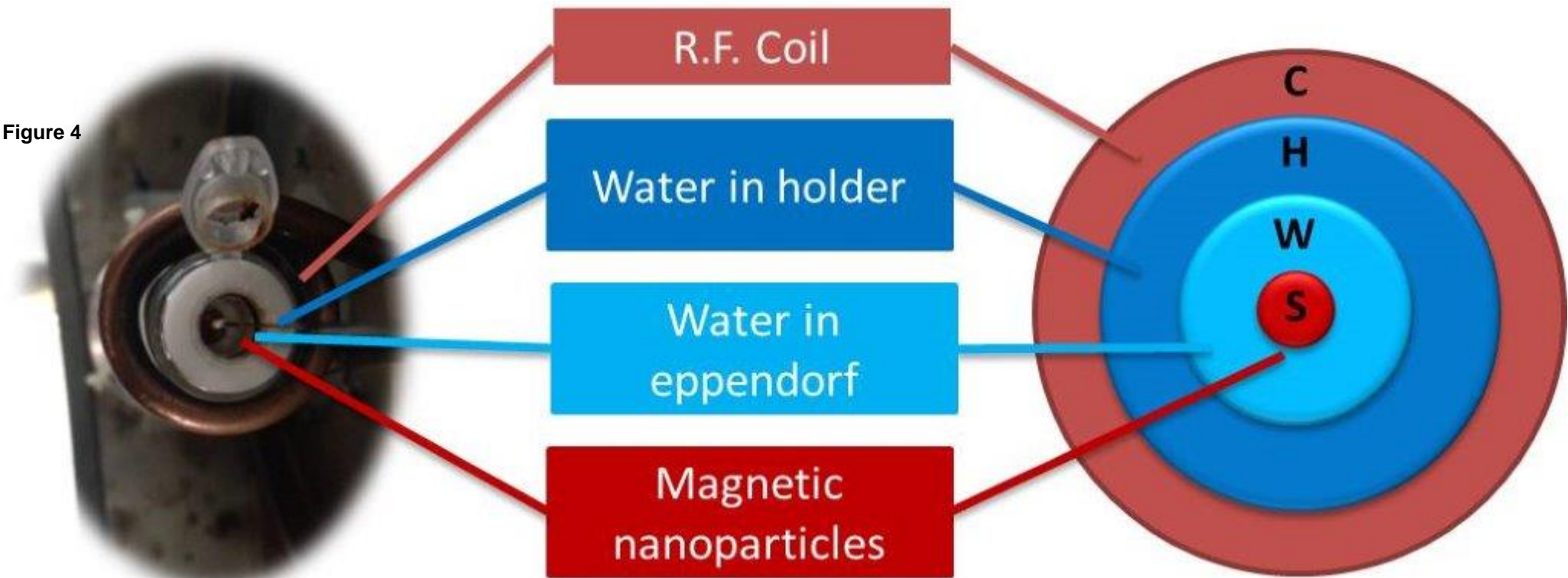
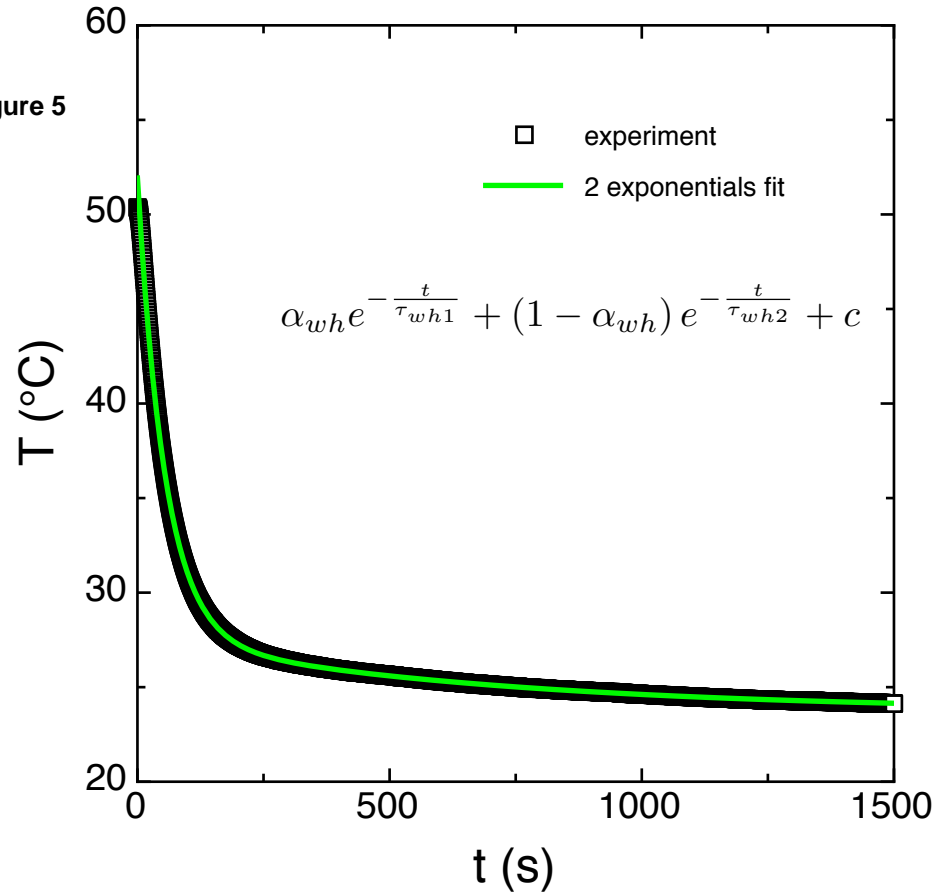
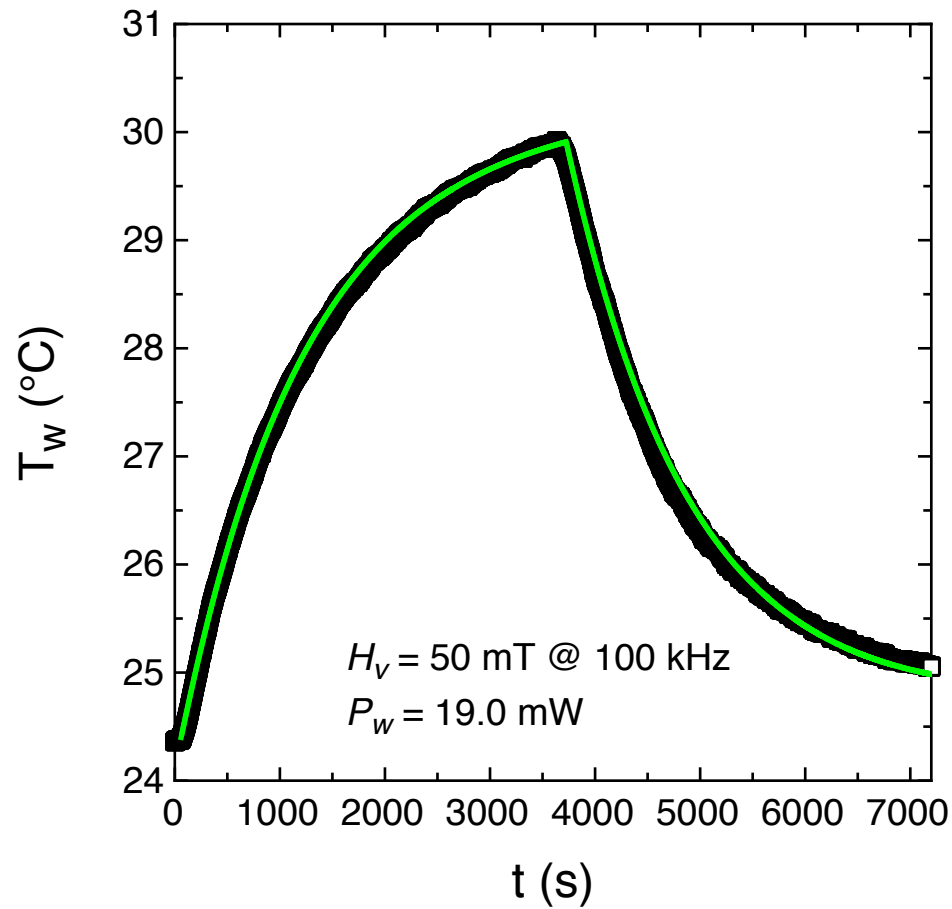
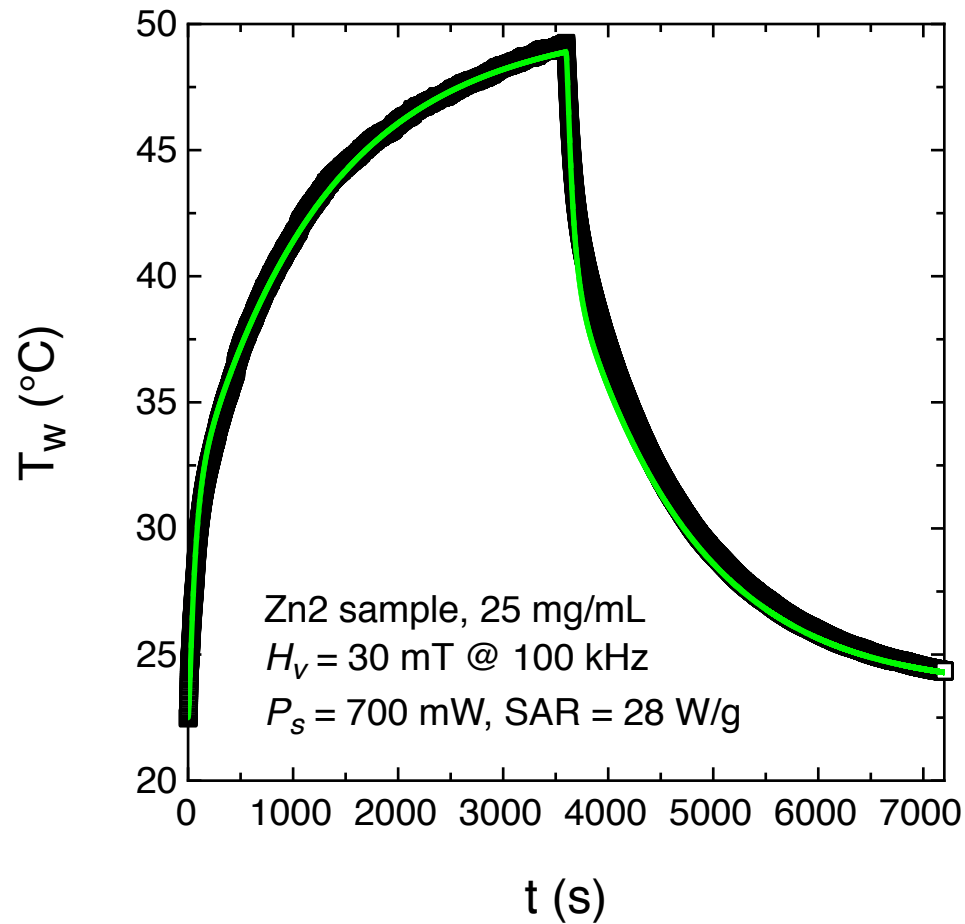
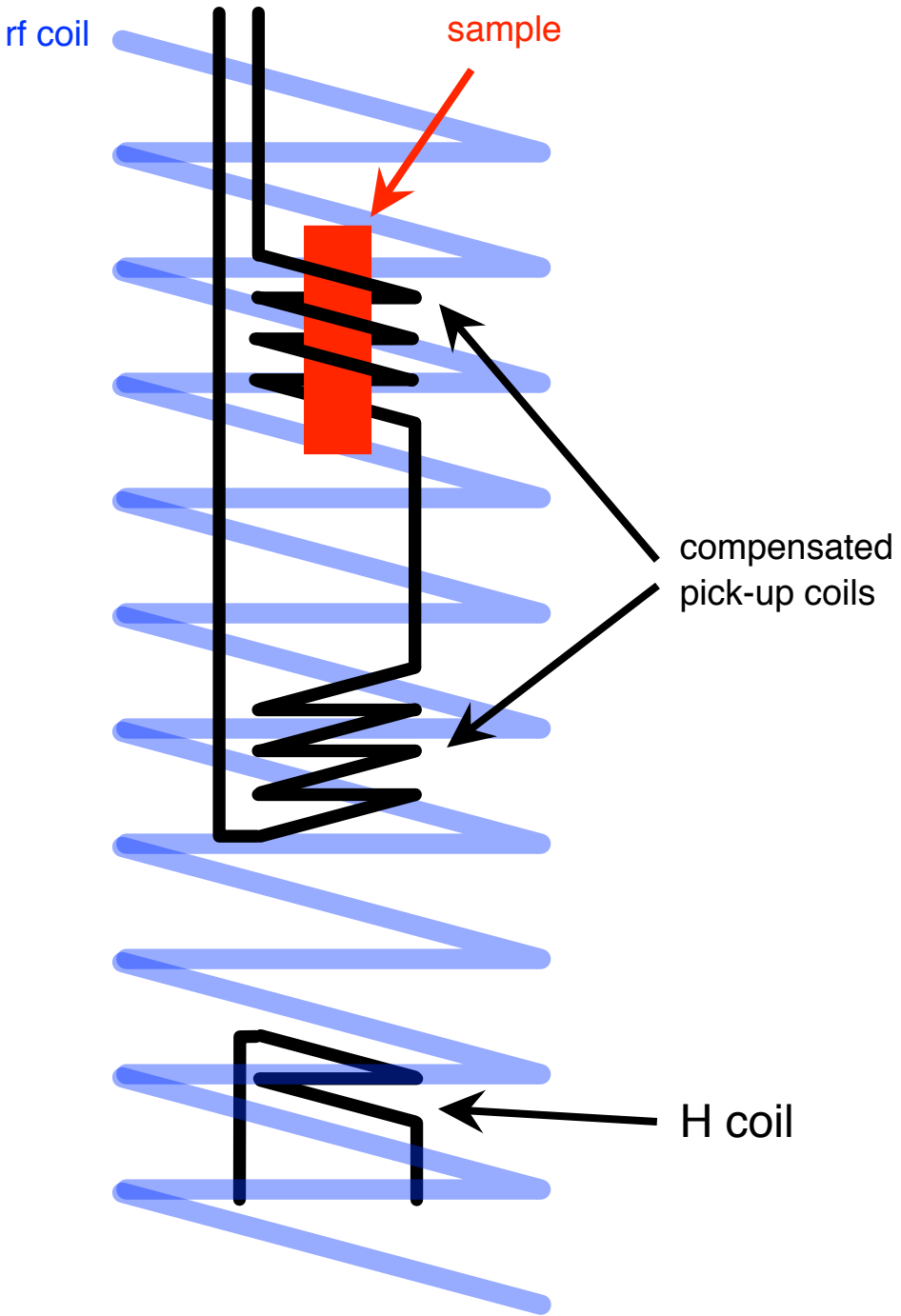


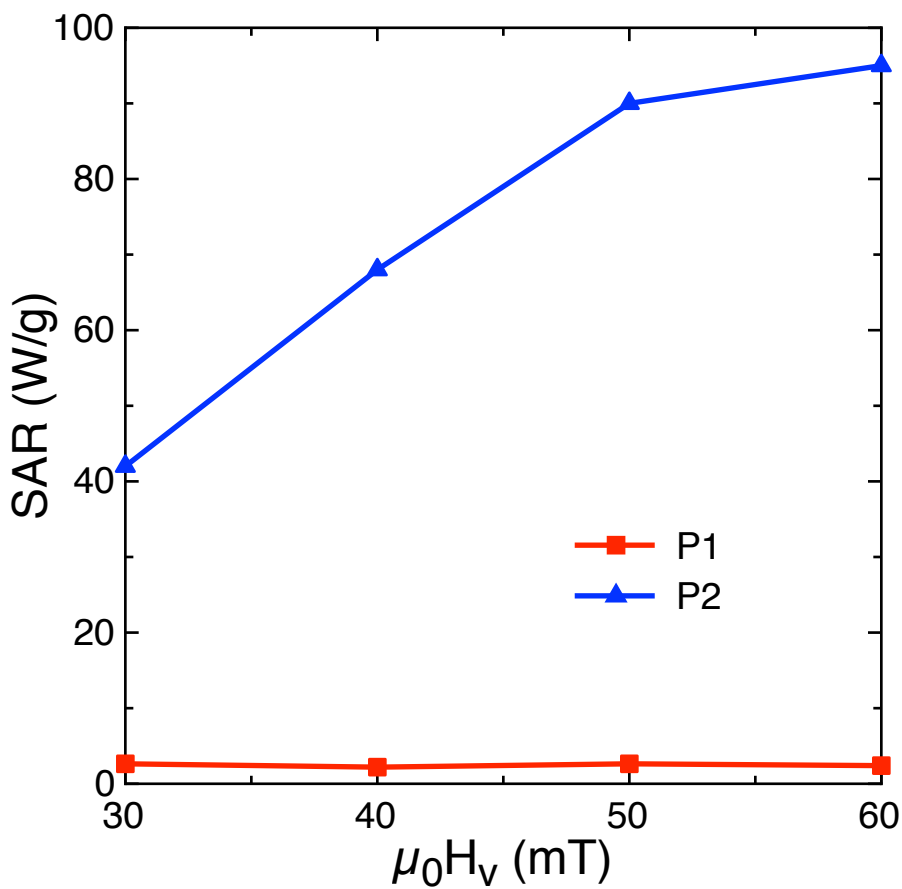
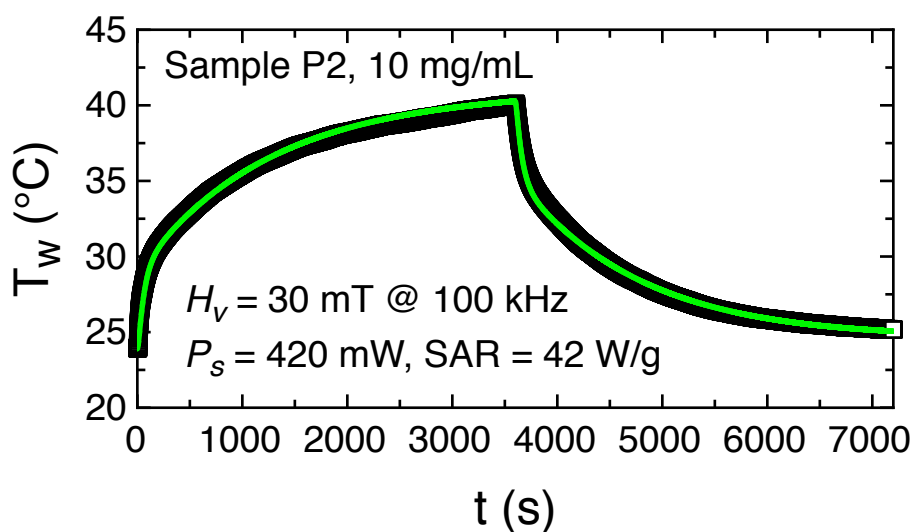
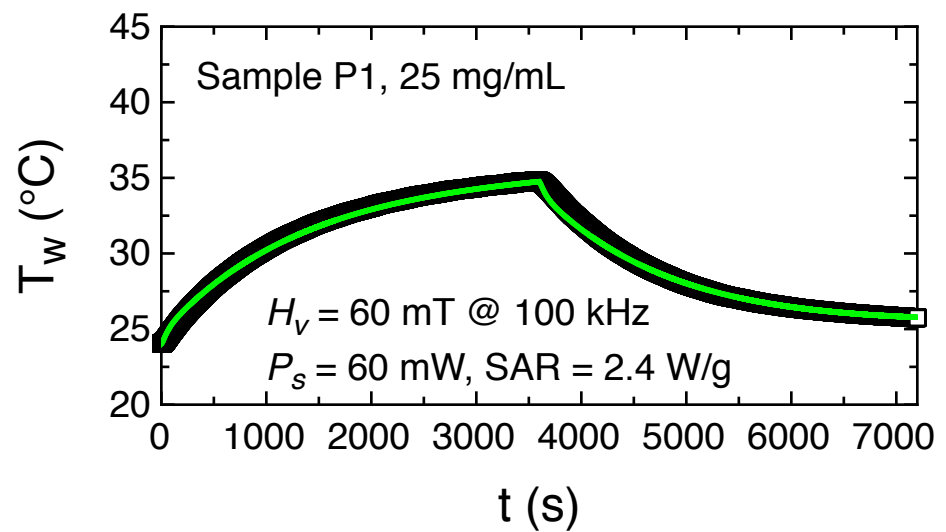
Figure 5

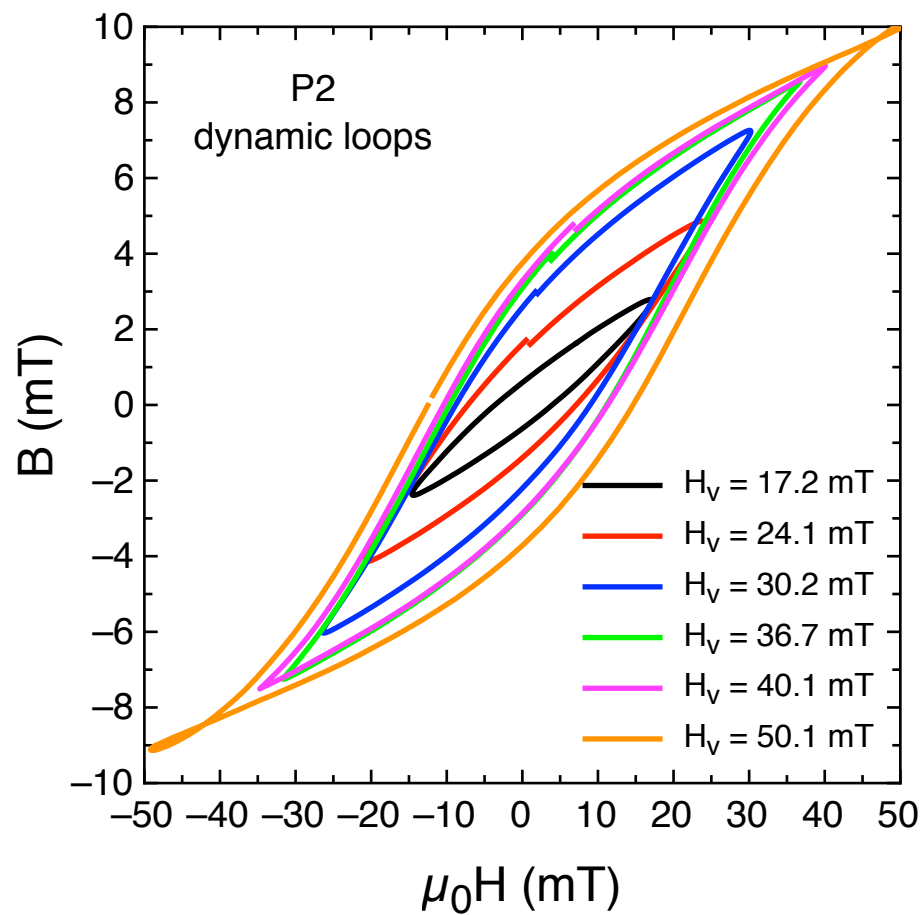
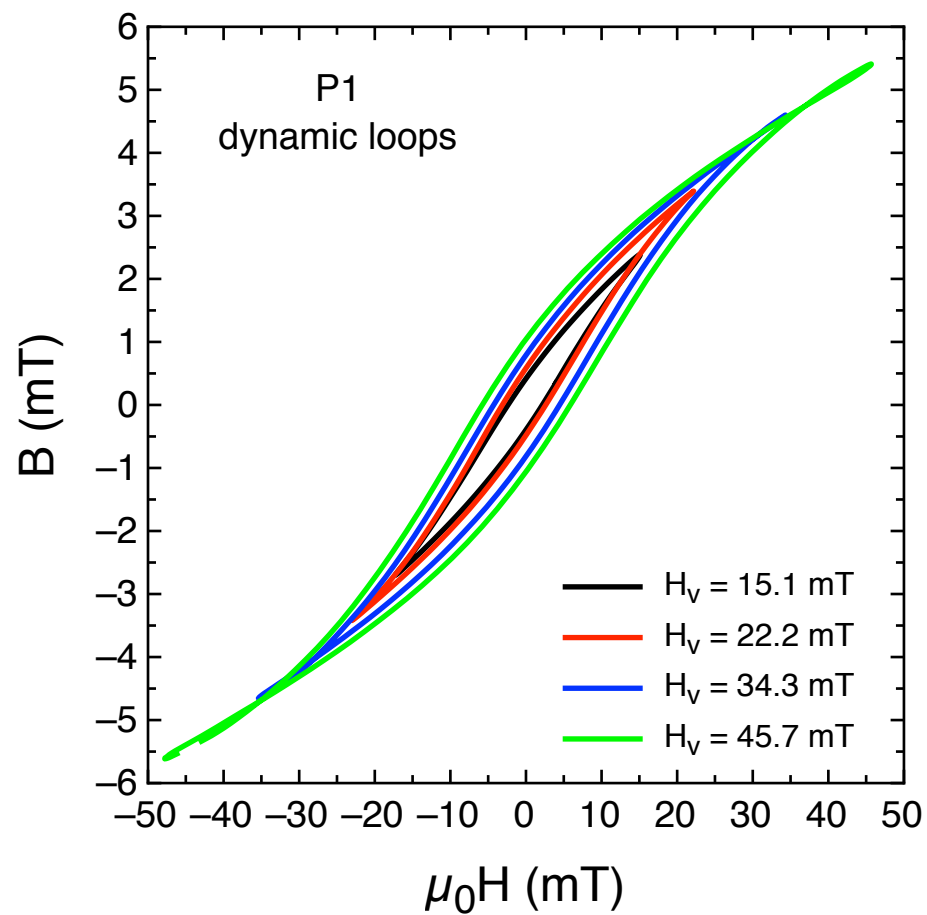
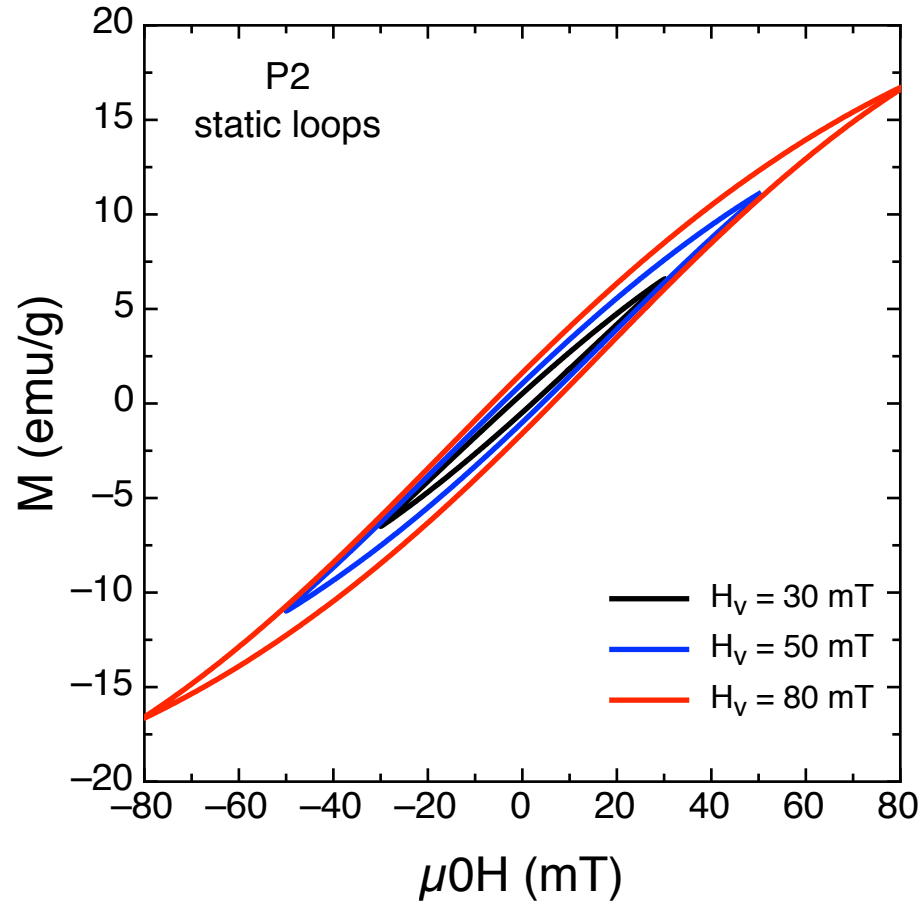


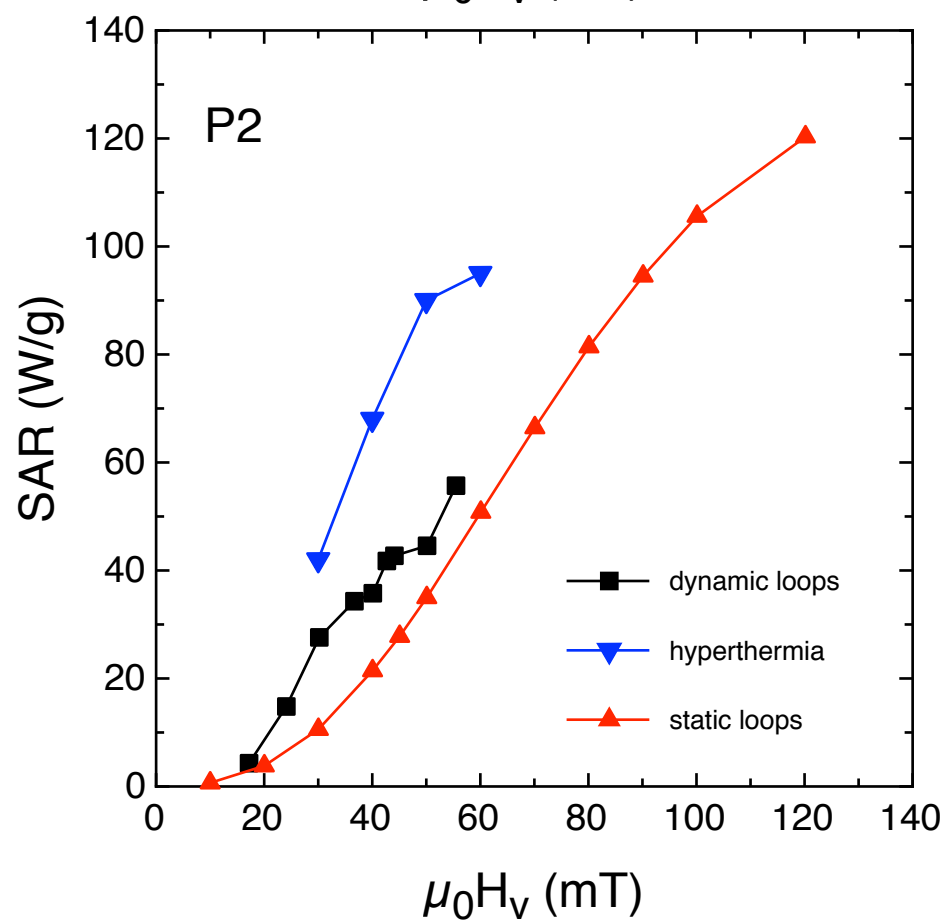
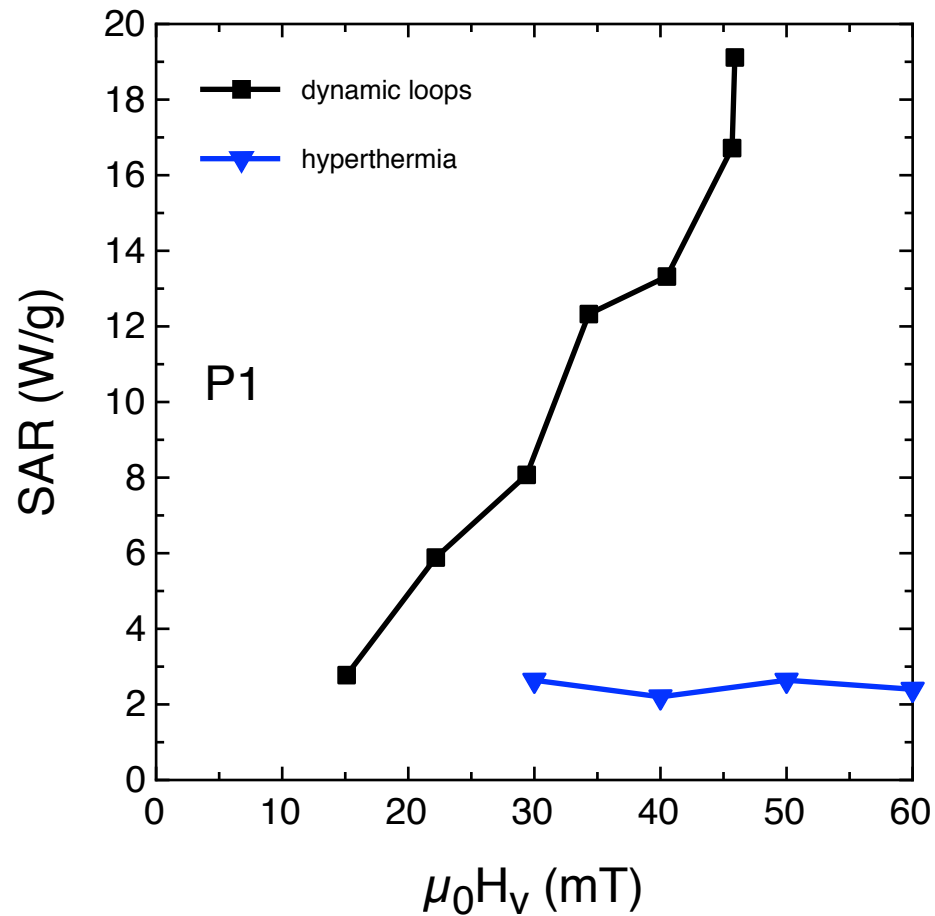


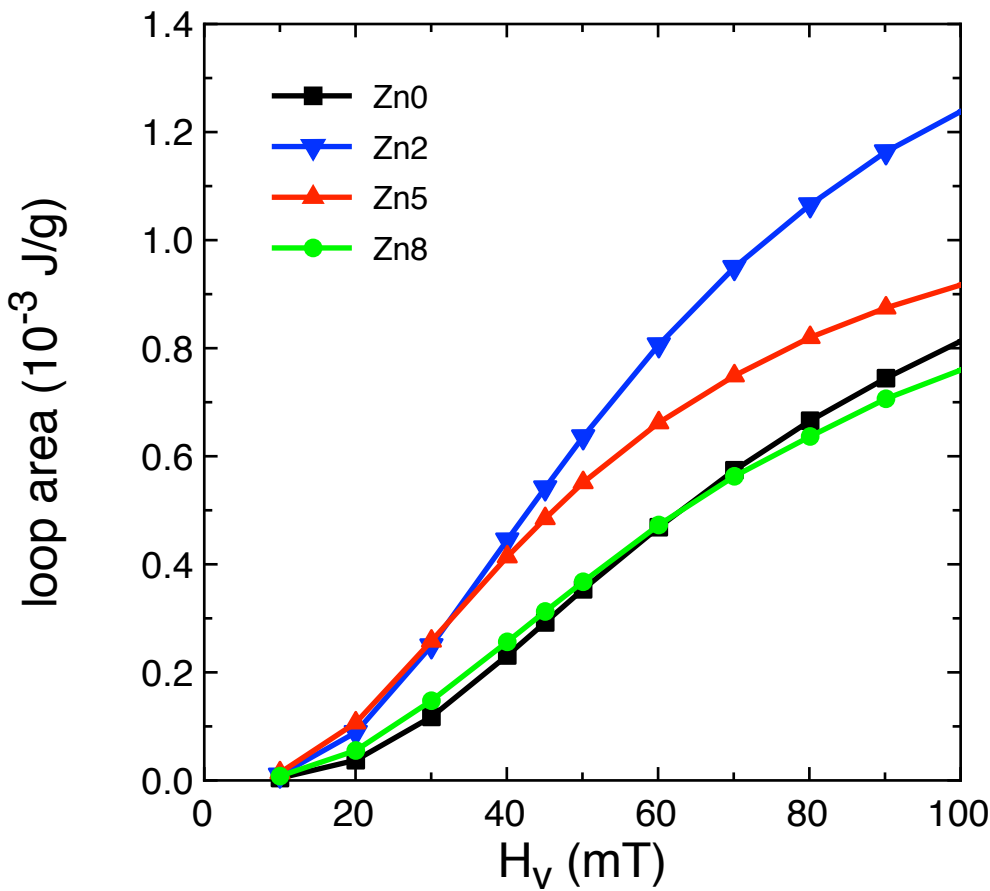


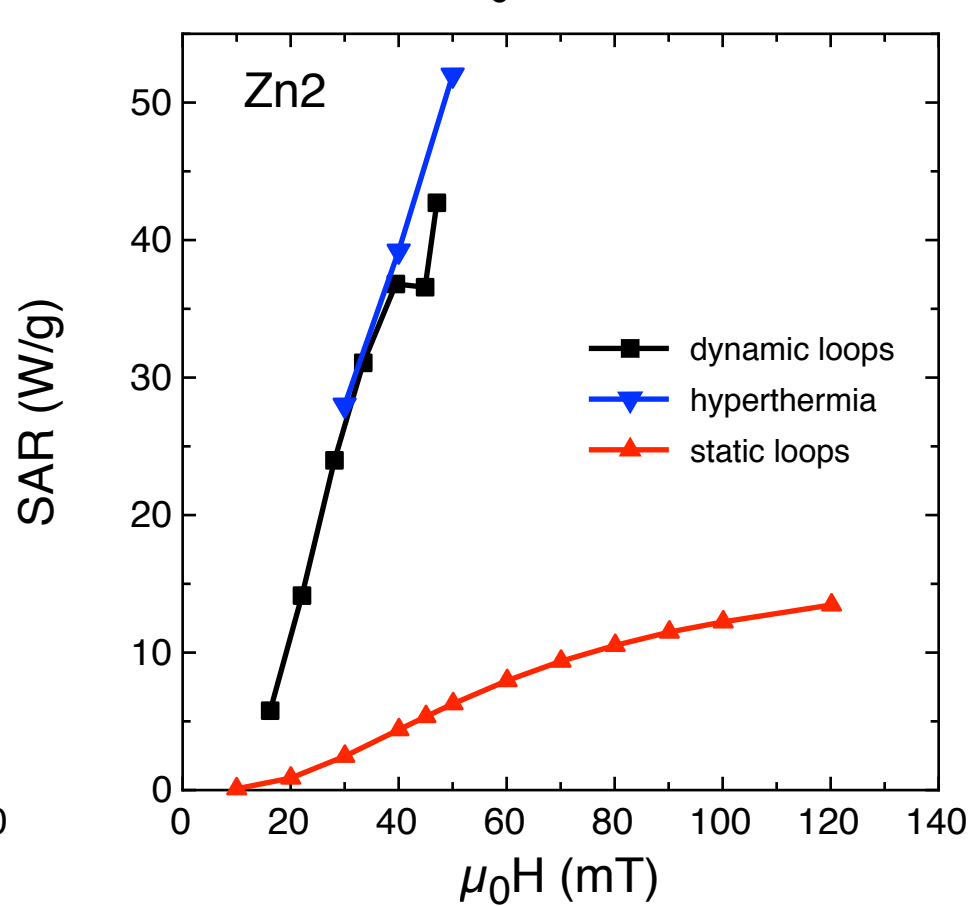
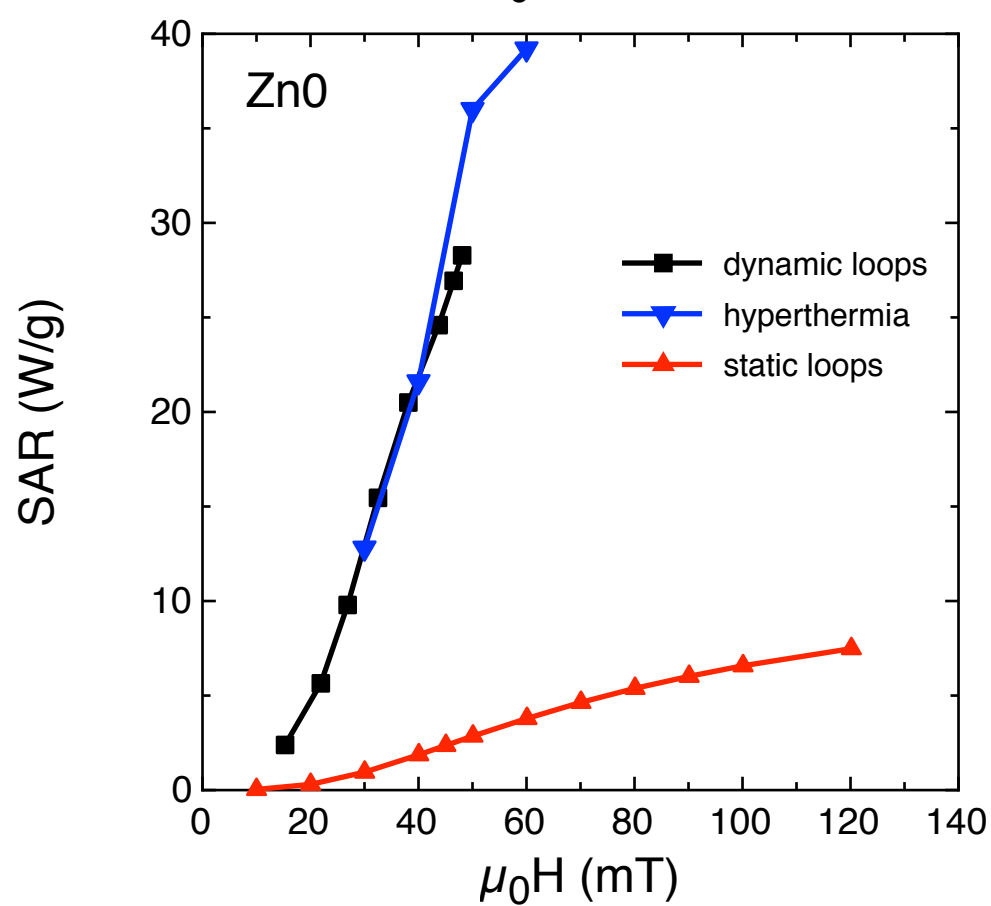
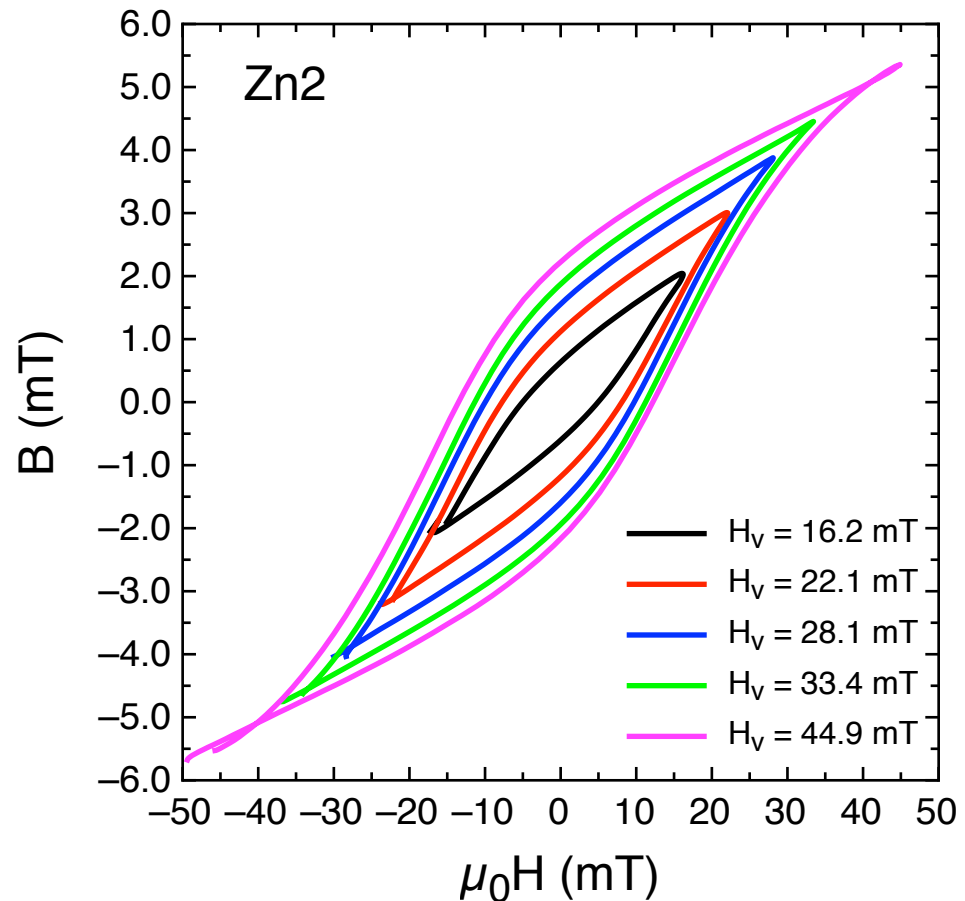
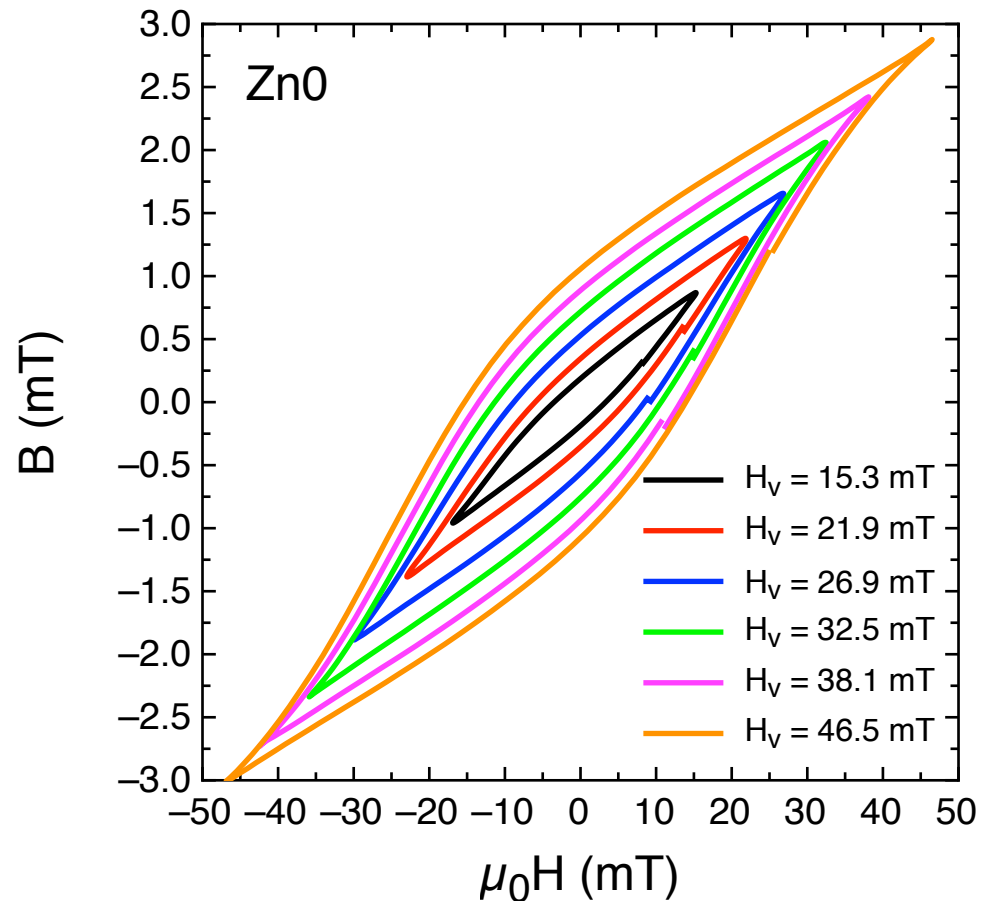












***Conflict of Interest form**

[Click here to download Conflict of Interest form: coi_disclosure_approved.pdf](#)